PRDM16 functions as a co-repressor in the BMP pathway to suppress neural stem cell proliferation

Li He[1], Jiayu Wen[2, *] and Qi Dai[1, *]

1 Department of Molecular Bioscience, the Wenner-Gren Institute, Stockholm University

2 Division of Genome Sciences and Cancer, The John Curtin School of Medical Research, The Australian National University and Australian Research Council Centre of Excellence for the Mathematical Analysis of Cellular Systems.

* Co-corresponding authors

Abstract

BMP signalling acts as an instructive cue in various developmental processes such as tissue patterning, stem cell proliferation, and differentiation. However, it is not fully understood how this signalling pathway generates different cell-specific outputs. Here we have identified PRDM16 as a key co-factor for BMP signalling. PRDM16 contributes to a repressive role of BMP signalling on neural stem cell (NSC) proliferation. We demonstrate that PRDM16 regulates the genomic distribution of BMP pathway transcription factors, the SMAD4/pSMAD complex, preventing the activation of cell proliferation genes. When *Prdm16* is lost, the SMAD complex relocates to nearby genomic regions, leading to abnormal upregulation of BMP target genes. This function of PRDM16 is also required for the specification of choroid plexus (ChP) epithelial cells. Through a single-cell resolution fluorescent *in situ* approach, we have observed that genes co-repressed by SMAD and PRDM16, such as *Wnt7b* and several cell cycle regulators, become overexpressed in *Prdm16* mutant ChP. Our findings elucidate a mechanism through which SMAD4 and pSMAD1/5/8 repress gene expression. Moreover, our study suggests a regulatory circuit composed of BMP and Wnt signaling, along with PRDM16, in controlling stem cell behaviors.

Introduction

Uncontrollable cell proliferation can lead to tumor growth, while premature differentiation can result in tissue degeneration. The balance between stem cell proliferation and differentiation is a crucial aspect in developmental and stem cell biology. BMP (Bone morphogenetic proteins) signaling is a key cell-signaling pathway in regulating stem cell proliferation and maintaining adult stem cell quiescence. Moreover, BMP signaling is essential in various cell specification processes [1].

The ability of a single pathway to play a diverse range of roles relies on context-specific transcriptional outputs. BMPs signal through two types of SMAD proteins: the receptor SMADs (R-SMADs) - Smad1, 5 and 8, and the co-SMAD protein SMAD4. Upon ligand binding, heterodimeric receptors like BMPRI and BMPRII phosphorylate R-SMADs, leading to the assembly and nuclear translocation of the SMAD complex with SMAD4. This complex then regulates gene expression by binding to enhancers of BMP target genes. Apart from transducing BMP signaling, SMAD4 is an essential effector in TGF-β/Activin signaling. In response to ligands such as TGF-β and Activin, SMAD4 associates with two other R-SMADs - phosphorylated SMAD 2 and 3, regulating downstream genes of the TGF-β/Activin signaling pathway. These SMADs recognize and directly bind to two main types of short DNA motifs in target enhancers via their N-terminal MH1 domain [2]. However, sicne the binding is generally weak, SMAD complexes rely on various co-factors such as transcription factors, co-activators and co-repressors to activate or repress target gene expression [3].

In the mammalian brain, BMP and Wnt signaling pattern the brain midline where an essential structure, the ChP, emerges. Neural epithelial cells at the presumptive ChP site lose neural potential and exit cell cycle. Only a small number of cells at the boarder of the ChP primordium and cortical hem (CH) persist as slowly dividing ChP progenitors, leading to the expansion of the monolayered ChP epithelial cells [4]. BMP signaling is essential for ChP epithelium specification. Conditional depletion of the BMP receptor *BMPr1a* diminishes ChP development [5], whereas ectopic BMP transforms neural progenitors into ChP cells [6]. Wnt signaling, peaking at CH, is also necessary for ChP epithelial cell specification [7]. Conditional depletion of ß-Catenin results in defective ChP, and overexpression of ß-Catenin expands CH at the expense of the ChP epithelium. These findings emphasize the importance of tightly controlling Wnt and BMP signaling levels for proper cell specification.

The PR domain-containing (PRDM) family protein PRDM16 determines cell fate specification in various cell types [8-14]. Previous studies, including our own, demonstrated that *Prdm16* knockout (KO) mouse brains show severely reduced ChP structures [15-17]. Interestingly, it was shown that PRDM16 can interact with TGF-ß pathway SMAD proteins *in vitro* and impact TGF-ß signaling output in craniofacial tissues [16,18]. PRDM16 is also a downstream effector of BMP signaling during brown adipocyte specification [19,20]. A recent study reported that PRDM16 and its ortholog PRDM3 (also known as Evi1) regulate Wnt signaling during craniofacial development in zebrafish [21]. These findings suggest that PRDM16 may be more broadly involved in regulating BMP/TGF-ß and Wnt signaling. However, the underlying molecular mechanisms remain unclear.

Consistent with its essential roles in normal development, mutations and dysregulation of *Prdm16* are linked with several human diseases, including those identified in the patients with 1p36 chromosomal aberrations and cardiomyopathy [22]. PRDM16 exhibits versatile functions at the molecular level, regulating chromatin accessibility and epigenetic states of its bound enhancers [13,15]. Depending on associated cofactors, PRDM16 can either repress or activate gene expression. This dual role poses a challenge when considering PRDM16 as a therapeutic target, as undesired outcome may occur. Thus, a comprehensive understanding of the regulatory roles of this protein in each specific process is crucial for effective disease treatment strategies.

In this study we have investigated the mechanisms that regulate the transition between stem cell proliferation and differentiation during ChP development. We show that *Prdm16* mutant ChP cells fail to exit cell cycle, a similar phenotype to when BMP signaling is abolished [5]. Using primary NSC culture, we dissected the molecular interaction of SMAD4/pSMAD1/5/8 proteins with PRDM16, and found that PRDM16 functions as a co-repressor that holds the SMAD complex at distal enhancers, repressing genes involved in cell proliferation. Finally, we validated that some of the co-regulated genes by BMP signaling and PRDM16 become de-repressed in the *Prdm16* mutant ChP. These findings uncover an essential function of PRDM16 in stem cell regulation and BMP and Wnt signalling.

Results

PRDM16 promotes cell cycle exiting of neural epithelial cells at the ChP primordium

To understand how *Prdm16* regulates ChP epithelial specification, we first investigated the expression of this gene in the developing mouse brain. At embryonic day 10.5 (E10.5), when BMP signaling specifies the presumptive ChP [5], *Prdm16* mRNAs and nuclear localization of the PRDM16 protein become detectable in this region (**Fig. 1A, supplementary Fig. 1A**). As previously shown, *Prdm16*^{cGT}, a *Prdm16* knockout allele (*Prdm16 KO*), displayed severely reduced ChP structure at E13.5 (**Fig 1B)** [15-17]. In the *Prdm16* KO brain, expression of the ChP marker gene, *Ttr*, is not only reduced in the lateral ventricle (tChPs) (**Fig. 1C**) but also in the fourth ventricle (hChP) (**Supplementary Fig. 1B**), suggesting that the function of PRDM16 is not area-restricted but generally required for ChP development.

To assess the overall patterning of CH and ChP region, we checked the expression of two marker genes, *Wnt2b* and *BMP4*, using conventional RNA *in situ* hybridization. The *Wnt2b* signal appeared normal in the mutant brain compared with the control at E11.5 and E12.5 (**Supplementary Fig. 1C**), suggesting that CH is not affected by *Prdm16* deletion. The level and range of *BMP4* expression also appeared comparable between wild-type and mutant brains. Thus, there is no overall patterning defect of ChP and CH in the *Prdm16* mutant.

However, the *Prdm16* mutant ChP epithelial layer remained as thick as the neural epithelium (**Fig. 1C, Supplementary Fig. 1C**). This phenotype prompted us to investigate cellular changes underlying defective ChP in the *Prdm16* mutant. We first examined cell proliferation by a 2-hour EdU labeling at E12.5. In control embryos, the ChP cells were mostly EdU negative and forming a monolayer, suggesting the majority of them had exited the cell cycle. In contrast, *Prdm16* mutant ChP cells remained highly proliferative (**Fig. 1D**). This result suggests the following possibilities: the ChP epithelium is not properly specified in the mutant, *Prdm16* mutant ChP cells are specified but cannot exit the cell cycle for differentiation, or both.

To assess these possibilities, we first examined cell type composition of *Prdm16* mutant ChP cells at E12.5. We stained control and mutant brain slices with the neuronal marker Doublecortin (Dcx). The control brain lacked Dcx-positive cells in the ChP, indicating that neural epithelial cells were specified into ChP epithelial cells, and thus lost neural potential (**Fig. 1E**). However, in the *Prdm16* mutant ChP, there were a number of Dcx-positive cells

lining along the basal side of the epithelium, suggesting continued neurogenesis. Additionally, we examined the stem cell marker SOX2. SOX2 is highly expressed in NSCs adjacent to the ChP epithelium, but its expression became significantly reduced in the presumptive ChP area (**Supplementary Fig. 1D**). Such reduction was abolished in the *Prdm16* mutant. Together, these results demonstrate that at E12.5 *Prdm16* depletion disrupted the transition from neural progenitors into ChP epithelia and arrested cells in proliferation.

We then wondered whether PRDM16 not only controls the specification of the ChP epithelium but also directly restricts cell proliferation. To investigate this, we examined *Prdm16* mutant ChP cells at a later stage. We performed a double S-phase labeling experiment by sequentially injecting EdU at E12.5 and BrdU at E13.5, then harvested the samples at E14.5. At this stage, the wild-type ChP had grown into an elongated and monolayered epithelium in which cells were mostly negative for EdU and BrdU. However, the *Prdm16* mutant ChP appeared as a clump of cells positive for EdU, BrdU or both (**Fig. 1F-G**). This result suggests that at a later stage the *Prdm16* mutant ChP epithelium can separate from the neuroepithelium but still cannot exit cell cycle to differentiate, confirming a direct role of PRDM16 on cell proliferation.

BMP signaling is a master regulator of ChP formation, and the BMP pathway mutant, Foxg1-cre::loxp*Bmpr1a,* also displayed ectopic cell proliferation in the developing ChP [5]. We then wondered whether PRDM16 interacts with the BMP pathway to restrict cell proliferation.

PRDM16 and BMP signaling collaborate to induce NSC quiescence *in vitro*

To examine the molecular interaction between PRDM16 and BMP signaling in regulating cell proliferation, we switched to using primary NSCs. It is known that BMP signaling maintains adult NSC quiescence *in vivo* and can induce proliferative NSCs into quiescence *in vitro* [23]. A previous study also reported that embryonic cortical NSCs are sensitive to BMP4 treatment, making them suitable for studying BMP downstream events [24]. Therefore, we established a cell culture assay to measure effects of BMP4 and PRDM16 on NSC proliferation and quiescence (**Fig. 2A**).

Unexpectedly, the PRDM16 protein became nearly undetectable when NSCs were cultured *in vitro* (**Supplementary Fig. 2A**), despite a high level of *Prdm16* mRNAs (**Supplementary Fig. 2B**). Given that the PRDM16 protein exclusively localizes in the nucleus of NSCs in embryonic brain tissues (**Fig. 1B**, **Supplementary Fig.1A** and [15]), our observation suggests that an

unknown mechanism controls the stability and nuclear localization of PRDM16 *in vivo*. Post-translational modification of PRDM16 has been reported as an important regulatory switch for PRDM16 function in brown adipocytes [25]. We speculate a similar mechanism in NSCs in the brain.

To overcome this issue and examine the potential molecular function of PRDM16 in NSC proliferation and gene regulation, we infected primary NSCs with a lenti-viral construct that constitutively expresses *3xNSL_Flag_Prdm16*. This resulted in a cell line expressing high levels of *Prdm16* mRNAs and detectable nuclear PRDM16 protein (**Supplementary Fig. 2A-B**), termed *Prdm16_expressing (Prdm16_E)*. For comparison, we cultured NSCs from *Prdm16* KO brains from the same developing stage and brain area, and also generated a cell line by infecting *Prdm16_ KO* cells with the same viral vector, expressing 3xNSL_Flag.

To measure cell proliferation rate, we labeled these cells with EdU and mKi67. Treating *Prdm16_E* NSCs with BMP4 resulted in a reduction in the number of cells positive for mKi67 or EdU (**Fig. 2B-D**). Following the washout step, *Prdm16_E* NSCs restored the numbers of EdU and mKi67 positive cells, indicating a return to the proliferative state, which confirms that BMP4 induces cell quiescence, a reversible state of non-proliferation. In contrast, a higher fraction of the *Prdm16*_KO cells failed to exit cell cycle after BMP4 addition, as evidenced by a less pronounced reduction of the population of mKi67 or EdU positive cells (**Fig. 2B-D**). It is worth noting that *Prdm16_KO* cells maintain the same properties with or without the control viral vector (**Supplementary Fig. 2C-F)**, so we used these two cell lines interchangeably.

Previous studies have shown that BMP4 can program ChP cell fate and activate ChP genes from neural progenitors *in vitro* [6]. To investigate whether PRDM16 facilitates BMP signaling in the induction of ChP genes, we measured the expression of *Ttr* using reverse-transcription followed by quantitative PCR (RT-qPCR). In NSCs expressing *Prdm16*, we observed an increase in *Ttr* mRNA expression upon BMP4 treatment, whereas *Prdm16*_KO NSCs and NSCs lacking the *Prdm16*_expressing construct showed no induction at all (**Fig. 2E and Supplementary Fig. 2G**).

Thus, similar to controlling ChP specification, both BMP signaling and PRDM16 are required for restricting NSC proliferation and ChP gene expression. We then proceeded to examine the molecular function of PRDM16 and BMP signaling in this context.

BMP signaling and PRDM16 cooperatively repress proliferation genes.

To understand how BMP signaling and PRDM16 suppress cell proliferation, we aimed to determine the transcriptional targets of SMAD4 and pSMAD1/5/8 in cells with and without BMP4. We first applied Cleavage Under Targets and Tagmentation (CUT&TAG) experiments using a PRDM16 antibody and the available SMAD antibodies to profile their genomic binding sites. The PRDM16 antibody worked efficiently, but none of the SMAD antibodies produced libraries with sufficient sequencing reads. Subsequently we employed chromatin immunoprecipitation followed by deep-sequencing (ChIP-seq) for the SMAD proteins. Given that SMAD4 forms a complex with SMAD2/3 only in response to TGF-β/activin-type ligands, we included an antibody targeting SMAD3 as a control for non-BMP4-induced SMAD4 binding. Thus, our experiment settings enabled us to profile genomic binding sites for PRDM16, SMAD4 and two types of R_SMADs under conditions with endogenous BMPs and TGF-β/Activin, as well as ectopic BMP4.

In *Prdm16_E* cells without BMP4, we identified several hundred to a few thousand ChIP-seq peaks for all three classes of SMAD proteins after normalizing to the input reads (FDR < 10%), indicating a modest level of endogenous BMP and TGF-β signaling in these cells (**Fig. 3A, Supplementary Fig. 3A-C**). Following BMP4 addition, pSMAD1/5/8 exhibited approximately a 750-fold increase in peak number, while the number of SMAD3 peaks increased by less than threefold (**Fig. 3A**, **Supplementary Fig. 3A**). Furthermore, in cells treated with BMP4, the pSMAD1/5/8 peaks largely overlap with the SMAD4 peaks, but much less with the SMAD3 peaks (**Supplementary Fig. 3B**). For example, pSMAD1/5/8 binds to two enhancers in the intronic region of *Prdm16*, with the binding intensity dramatically increased in response to BMP4 (**Supplementary Fig. 3D**). This suggests that *Prdm16* itself is a transcriptional target of BMP signaling. Indeed, *Prdm16* mRNA levels were elevated by BMP4 in wild-type but not *Prdm16_KO* cells (**Supplementary Fig. 2B**). By contrast, SMAD3 showed little ChIP-seq signal in the *Prdm16* gene locus even in the presence of BMP4. These results confirm that the response of pSMAD1/5/8 is specific to BMP4, while SMAD3 is generally unresponsive to BMP4. The gained Smad3 sites likely result from an indirect effect of BMP signaling.

To evaluate the regulatory activity of SMAD4/pSMAD1/5/8 in NSCs, we determined the state of transcription activation using H3K4me3 CUT&TAG signals at annotated gene transcription start sites (TSS) in BMP4-treated and untreated *Prdm16_E* cells. As cell identity genes are

known to be marked by extended breadth of H3K4me3 [26], we reasoned that compared to RNA-seq, which measures all gene products, changes in the H3K4me3 signal at the promoter might bias toward cell identity genes between proliferation and quiescence states. Thus, we determined all BMP4-repressed and activated genes by measuring changes in the H3K4me3 CUT&TAG read coverage at annotated TSS in BMP4-treated *Prdm16_E* cells compared to untreated, identifying 282 up-regulated and 429 down-regulated genes (**Fig. 3B**) ($P<0.01$). To pinpoint genes directly regulated by SMAD4 and pSMAD1/5/8, we intersected the dysregulated genes with those whose regulatory regions contain overlapping SMAD4 and pSMAD1/5/8 ChIP-seq peaks. This analysis led to the identification of 145 up-regulated and 184 down-regulated SMAD4 and pSMAD1/5/8 target genes.

To elucidate the function of BMP-regulated targets, we performed gene ontology (GO) analyses for the genes that changed expression in response to BMP4 in *Prdm16_E* cells and were also bound by SMAD4 and pSMAD1/5/8. Remarkably, the downregulated genes (BMP4-repressed genes), but not the up-regulated genes (BMP4-activated genes), showed significantly enriched functional categories, with nearly all GO terms related to cell proliferation/cell cycle (**Fig. 3C)**. A recent study reported that BMP2-induced genes are enriched for neuronal and astrocyte differentiation [27], while our analysis did not identify these categories. One possibility for the discrepancy is that we overexpress *Prdm16* in cultured NSCs, which may reinforce BMP signaling activities in cell proliferation. Other possibilities could be the use of different BMP ligands (BMP4 versus BMP2), differences in the origin of NSC culture (ours was from E13 instead of E11 and E14), or different profiling methods (H3K4me3 versus RNA-seq).

To identify PRDM16-repressed and activated genes under active BMP signaling conditions, we compared changes of H3K4me3 coverage at TSSs between BMP4-treated *Prdm16_KO* cells and BMP4-treated *Prdm16_E* cells. We found approximately twice as many up-regulated genes (240) as down-regulated genes (132) (**Fig. 3D**), suggesting that the cooperative activity of PRDM16 and BMP signaling mainly represses gene expression. We further overlapped the 184 genes repressed by BMP4 and the 240 genes repressed by PRDM16, identifying 31 common ones. These 31 genes displayed low H3K4me3 coverage in *Prdm16_E* cells with BMP4 but higher H3K4me3 signal in both *Prdm16_KO* cells treated with BMP4 and untreated *Prdm16_E* cells (**Fig. 3E).**

Next, we attempted to validate whether changes in TSS H3K4me3 intensity correspond to changes in mRNA levels, by conducting RT-qPCR for selected genes whose function is

associated with cell proliferation: *Wnt7b*, *Mybl2*, *Id3*, *Spc24* and the three *Spc24*-related genes (*Spc25*, *Ndc80* and *Nuf2*) (**Fig. 3F-G, Supplementary Fig. 3E-K**). SPC24 forms the NDC80 kinetochore complex along with three other proteins: SPC25, NDC80 and NUF2 [28] (Illustrated in **Supplementary Fig. 3H**), and their function is essential for chromosome segregation and spindle checkpoint activity. Notably, *Spc25*, *Ndc80* and *Nuf2* appeared repressed by PRDM16 and BMP4 based on changes in H3K4me3 at the TSS (**Supplementary Fig. 3E**), despite not being identified as the top 31 candidates. mRNA levels for most of the tested genes followed a similar pattern to the H3K4me3 intensity: BMP4-treated *Prdm16_E* cells showed the lowest expression, while either the loss of *Prdm16* or absence of BMP4 led to upregulation. *Spc24* gene products showed minimal amplification in qPCR, likely due to poor primer sequence quality or unstable mRNAs. Another exception is *Id3* whose expression increased upon BMP4 treatment or *Prdm16* depletion, indicating PRDM16 repressing *Id3* but BMP4 inducing *Id3*. However, the activation of *Id3* by BMP4 is significantly stronger in *Prdm16_KO* cells than that in *Prdm16*_E cells, suggesting that BMP signaling normally activates *Id3* but PRDM16 suppresses such activation. In contrast, *Cdkn1a*, a target gene of TGF-β pathway encoding the cell cycle inhibitor P21, exhibited consistent H3K4me3 coverage and mRNA levels across BMP4 treated and non-treated cells, as well as between *Prdm16_E* and *KO* cells (**Fig. 3F-G**), confirming that neither PRDM16 nor BMP signaling influences *Cdkn1a* expression in NSCs.

PRDM16 assists genomic binding of SMAD4 and pSMAD1/5/8

To understand how PRDM16 interacts with BMP signaling, we integrated PRDM16 CUT&TAG data with SMAD ChIP-seq data, focusing on assessing how PRDM16's influence on the genomic binding of SMAD proteins.

The SEACR peak caller software [29] identified 3337 and 7639 PRDM16 CUT&TAG common peaks from four replicates of BMP4-treated and untreated *Prdm16_E* samples (FDR < 10%, see Methods), respectively (**Fig. 4A**). Upon BMP4 treatment, there were 5936 lost and 1634 gained PRDM16 CUT&TAG peaks, suggesting that PRDM16 regulates a distinct subset of genes in proliferating versus quiescent NSCs. Samples from *Prdm16_KO* cells lacked these sites, confirming the specificity of the PRDM16 CUT&TAG signal (**Fig. 4B**).

From our overlapping analyses (see Methods), we found that over 50% of SMAD4 and pSMAD1/5/8 binding peaks were consistent in *Prdm16_E* and *Prdm16_KO* cells (**Supplementary Fig. 4A-B**), indicating that deletion of *Prdm16* does not affect general

genomic binding ability of these proteins. Using Homer's mergePeaks function with PRDM16 CUT&TAG and SMAD ChIP-seq data, we identified co-bound sites by PRDM16 and SMAD proteins in BMP4-treated *Prdm16_E* cells. PRDM16 CUT&TAG peaks mainly overlap with SMAD4 and pSMAD1/5/8 peaks, but not much with SMAD3 peaks (**Supplementary Fig. 4A-C**). This result suggests that PRDM16 mainly collaborates with the SMAD4/pSMAD1/5/8 complex but not the SMAD3/SMAD4 complex in cells with high levels of BMP4.

Further examination of SMAD4 and pSMAD1/5/8 binding revealed significantly lower enrichment of SMAD4 and pSMAD1/5/8 at PRDM16 co-bound sites in *Prdm16_KO* cells compared to *Prdm16_E* cells (**Fig. 4C**) (P=2.5E-6, and P=4.7E-3, respectively, two-tailed *t*-test). As a control, the SMAD4 and pSMAD1/5/8 sites without PRDM16 co-binding did not show such change (P>0.05). This result suggests that SMAD binding to these sites depends on PRDM16.

To validate the co-binding of SMAD4 and PRDM16, we selected the candidate loci, *Wnt7b* and *Id1* (**Fig. 4D-E**) and applied sequential ChIP-qPCR. This experiment confirmed simultaneous binding of SMAD4 and PRDM16 to the same DNA molecules at these loci (**Supplementary Fig. 4D**), as SMAD4 was more enriched in the chromatin pulled by the PRDM16 antibody compared to the IgG control. Additionally, ChIP-qPCR confirmed reduced SMAD binding at the SMAD/PRDM16 co-bound site in *Prdm16_KO* cells compared to *Prdm16_E* cells (**Fig. 4F-G**). Thus, PRDM16 enhances genomic binding of the SMAD proteins to specific genome regions.

PRDM16 facilitates SMAD4 binding to regions enriched for SMAD palindromic motifs

We then wondered whether there is sequence feature that distinguishes the regions co-bound by SMADs and PRDM16 from those only bound by SMADs. To this end, we checked SMAD-bound regions with PRDM16 binding and those without for two types of SMAD4 binding motifs [3]. Together with pSMAD1/5/8 or pSMAD3, SMAD4 may bind to a palindromic motif, GTCTAGAC or direct repeats of GTCT like GTCTGTCTGTCT [30-32]; together with pSMAD1/5/8, SMAD4 associates with GC-rich SBEs (SMAD-binding elements) including GGCGCC-AN4-GNCV and GRCGNCNNNNNGTCT [33-35]. We calculated occurrence frequency of each of these motifs in binned SMAD4 ChIP-seq peaks from *Prdm16_E* cells treated with BMP4 (bin 1 to 5 with low to high peak scores, **Fig. 4H**). Interestingly, the palindromic motif is the most enriched one. Its occurrence frequency increases with peak scores,

but becomes lower in the SMAD4 peaks absent for PRDM16 co-binding. The frequency of the GTCT-triplet motif also increases with higher SMAD4 peak scores, while there is no reduction in regions without PRDM16 binding. The two GC-rich motifs show a distinct trend: they are not as highly enriched, their frequencies do not increase with higher SMAD4 peak scores, and the occurrence frequency in PRDM16 co-bound regions is either comparable to or even lower than the regions without PRDM16 binding. Together, this result suggests that PRDM16 may separate the SMAD4/pSMAD1/5/8 proteins into two types of genomic regions, one enriched for the palindromic motif where PRDM16 is present and the other with the GC-rich motifs.

SMAD4 and pSMAD1/5/8 switch genomic locations in the absence of PRDM16

Our careful inspection on the *Wnt7b* and *Id1* loci surprisingly revealed that there are multiple ectopic SMAD4 and pSMAD1/5/8 peaks in the *Prdm16* mutant sample (arrow-indicated peaks in **Fig. 5A-B**). We then globally assessed the extent of ectopic SMAD binding surrounding the SMAD/PRDM16 co-bound sites by quantifying differential SMAD binding intensity between *Prdm16_KO* and *Prdm16_expressing* cells (**Fig. 5C,** FDR < 10%). In agreement with the metaplots (**Fig. 4C**), all of the SMAD/PRDM16 co-bound sites (blue dots) showed reduced ChIP-seq read coverage in *Prdm16_KO* cells. By contrast, the flanking regions within the 200kb range of a co-bound site (red dots) displayed a trend of increase of SMAD binding in *Prdm16_KO* cells. This result agrees with the aforementioned motif analysis that PRDM16 helps to localize the SMAD complex at specific genomic regions, and it also suggests that without *Prdm16*, the SMAD factors are partly redirected to neighboring genomic regions.

AP1 is the potential co-factor that interacts with relocated SMAD proteins

We intended to find out how SMAD4 and pSMAD1/5/8 relocate to ectopic sites in the absence of *Prdm16*. By running *de novo* motif discovery (see Methods), we identified a number of significantly enriched DNA motifs from pSMAD1/5/8 and SMAD4 ChIP-seq peaks in *Prdm16_E* and *Prdm16_KO* cells (**Fig. 5D-E**). Interestingly, in addition to the known SMAD motifs, the only other motif identified in both pSMAD1/5/8 and SMAD4 peaks from *Prdm16_KO* cells but not *Prdm16_expressing* cells is the AP1 motif. Furthermore, the AP1 motif is more frequently found in the pSMAD1/5/8 and SMAD4 regions lacking PRDM16 binding than those with PRDM16 binding (Supplementary **Fig. 4E**). The interaction between the AP-1 complex with the SMAD proteins was reported previously [36]. Our result implies that AP-1 is a potential cofactor for the SMAD proteins in the absence of *Prdm16*. To validate this

finding, we performed ChIP-qPCR with an antibody against c-FOS, one of the subunits of AP1, on *Prdm16_E* and *KO* cells. Supporting the global analyses, c-FOS is enriched in the Smad4-bound regions at the *Wnt7b* and *Id3* loci in the *Prdm16_KO* condition (**Fig. 5F-G**). There is little c-FOS binding to these regions in cells expressing *Prdm16*, suggesting that there is cooperativity of SMAD and AP-1 which facilitates each other's binding when PRDM16 is absent. Alternatively, PRDM16 may suppress genomic accessibility of these regions for SMAD and AP-1 proteins, a function we reported for PRDM16 in cortical NSCs [15].

Together, our genomic data and validation suggest an enhancer switch model (**Fig. 5H)**: PRDM16 assists SMAD protein binding to repressive cis-regulatory elements that are enriched for GTCTAGAC palindromic motifs; loss of PRDM16 results in genomic relocation of SMAD proteins, presumably via the association with coactivators such as AP1; the consequence of SMAD relocation is de-repression of cell proliferation regulators.

SMADs and PRDM16 co-regulated genes in NSCs are repressed in the developing ChP

Next, we wondered whether some of the genes co-regulated by PRDM16 and BMP signaling in NSC culture (**Fig. 3C**) are involved in ChP development, an *in vivo* setting where BMP signaling [5] and PRDM16 (**Fig. 1**) restrict NSC proliferation. To address this, we first examined expression of the 31 genes in the developing mouse brain by taking advantage of the published single cell RNA-seq (scRNA-seq) data [37]. We selected a number of cell clusters based on marker gene expression from E12.5 mouse brain, including the ChP epithelial cell clusters (*Ttr* positive), CH clusters (BMP4 positive but *Ttr* negative) and a few forebrain-specific radial glia (RG) clusters (Sox2/Hes5 positive) (**Fig. 6A**). Among these genes, six show no expression, and five have weak expression in the examined clusters (**Supplementary Fig. 5A**). The remaining twenty genes display a moderate to high level of expression in at least one cluster. Interestingly, these genes are generally more lowly expressed in the ChP clusters than the neural clusters (CH and RG) (**Fig. 6A**), suggesting that their expression is suppressed in the ChP. To identify which of these genes are directly regulated by PRDM16, we performed CUT&TAG assays using the PRDM16 antibody on dissected dorsal midline tissues that mainly contain CH and the ChP (**Fig 6B** and **Supplementary Fig. 5B**) and identified 3238 common peaks from three biological replicates. We then manually inspected the 31 gene loci for PRDM16 CUT&TAG peaks pairing with the target gene TSS using the browser Embryonic Mouse Brain Epigenome Atlas [38]. This confirmed that most of these genes (Text in black in **Fig. 6A** and **Supplementary Fig. 5A**) have at least one PRDM16 binding peak in their promoter-linked enhancers.

For instance, the *Wnt7b* region has two PRDM16 binding peaks (**Fig 6C**), with the intronic one is unique to the dorsal midline tissue. The level of Wnt signaling was shown to be critical for ChP specification [7], and Wnt signaling promotes proliferation of NSCs [39]. Thus, *Wnt7b* is a potential target of PRDM16 in the developing ChP.

PRDM16 represses *Wnt7b* and Wnt activity in the developing ChP

We sought to determine which of the identified genes from NSC culture are regulated by PRDM16 in the developing ChP. In addition to *Wnt7b*, several other Wnt ligands are expressed in the CH and ChP region [40]. For example, *Wnt3a* is expressed in the dorsal-midline region but not in the forebrain, which explains why it was not identified from the forebrain-derived NSC datasets. Although there is no PRDM16 CUT&TAG peak within the *Wnt3a* locus in cultured NSCs, a PRDM16 CUT&TAG peak is present in the intronic region of *Wnt3a* in the dorsal midline tissue (**Supplementary Fig.5C**). We thus examined the scRNA-seq data [37] and confirmed that multiple components in the Wnt and BMP pathways are present in the CH and ChP clusters (**Supplementary Fig.5D**). To systematically measure expression changes of PRDM16 target genes in the *Prdm16* mutant brain, we applied a multiplexed fluorescent *in situ* approach, Single-Cell Resolution in Situ Hybridization On Tissues (SCRINSHOT) [41]. In this method each mRNA molecule is hybridized with three gene-specific padlock probes and visualized by florescent dye-conjugated detection probes. A dot of fluorescent signal corresponds to one mRNA molecule, allowing quantitative measurement of gene expression in single cell resolution.

We designed probes for ten Wnt and five BMP pathway components, other genes that are co-repressed by BMP and PRDM16 in NSC culture, as well as cell-type specific markers (the ChP marker gene *Ttr* and *Foxj1*, the neural progenitor markers *Sox2*, *Hes5* and *Zbtb20*, and the neuronal marker Ngn2), and conducted SCRINSHOT in three pairs of control and *Prdm16* mutant brains.

In the control brain, the *Ttr* and Foxj1 probes detect the ChP epithelium but not the adjacent tissues at E11.5 and E12.5, confirming the signal specificity of SCRINSHOT. Several Wnt (*Wnt2b*, *Wnt7b*, *Wnt5a*, *Wnt3a*, *Fzd10* and *Axin2*) and BMP components (*BMP4* and *BMP7*) also display tissue specificity: the Wnt genes are more enriched at CH while the BMP genes are more at the ChP. The representative images from E11.5 and E12.5 samples are presented in

Fig. 7A-B. Except *Wnt2b*, the other tested *Wnt* genes exhibit low expression in the ChP cells, consistent with the notion that Wnt signaling is present and required at the ChP [7].

Next, we quantified expression changes of these genes in *Prdm16* mutant CH and ChP cells. As expression of *Wnt2b* was relatively unchanged in the mutant (**Supplementary Fig. 1** and **Fig. 7A**), we used *Wnt2b*-expressing cells to define the CH cells and those expressing *Ttr* to define ChP cells in the wild-type brain slice. There were about 110 cells in each region of one brain slice. Because the mutant brain slice showed little *Ttr* signal, we only used the *Wnt2b*-expressing cells to define the anterior border between CH and neocortex and included 110 cells under the border for the CH cells, and the further 110 cells for the mutant ChP cells, as shown in the images with DAPI and cell outlines (**Fig. 7A and Fig. 7D**). We then measured the dot count of each gene in these 220 cells in each sample, and summarized the changes from three pairs of animals in the violin plots (**Fig. 7C** and **Supplementary Fig. 6A**). Expression of *Ttr* and *Foxj1* is severely reduced, while *Sox2*, *Hes5* and *Ngn2* all become upregulated in the mutant ChP, indicating a fate transformation of ChP epithelial to neural cells. This agrees with our immunostaining and conventional *in situ* results (**Fig. 1** and **Supplementary Fig. 1**). Similar to BMP4, other BMP components we tested including *BMP7*, *Smad6*, *Smad7 and Nog* are unchanged, suggesting that PRDM16 is not an upstream regulator of the BMP pathway.

Moreover, *Wnt3a* and *Wnt7b* are significantly upregulated in the *Prdm16* mutant ChP (**Fig. 7B-E** and **Supplementary Fig. 6A-C**). In line with this, the Wnt target gene *Axin2* is also upregulated, indicating aberrantly elevated Wnt signaling in the *Prdm16* mutant ChP. Thus, the normal function of *Prdm16* represses WNT signaling in the developing ChP.

Levels of Wnt activity correlate with cell proliferation in the developing ChP and CH

We further assessed the relationship between Wnt signaling and cell proliferation in the ChP and CH at E12.5, by correlating expression levels of *mKi67* with *Wnt3a*, *Wnt7b* and *Axin2* levels in wild-type and mutant samples. A significant increase of *mKi67* expression in *Prdm16* mutant ChP cells at E12.5 is accompanied by significantly increased Wnt gene expression (**Fig. 7F** and **Supplementary Fig 6B-C**). In contrast, little or no increase of *mKi67* signal is found in the mutant CH, suggesting that the effect of PRDM16 is mainly cell-autonomous. We then performed linear regression and Pearson correlation analyses to assess correlations between ChP markers, BMP and Wnt genes. Interestingly, the level of *Axin2* best correlates the level of m*Ki67*, even better than that with other Wnt genes in both wild-type ($r = 0.46$; $p < 2.2$ E-35)

and mutant (r= 0.56; p < 1.6 E-55) CH and ChP cells **(Fig. 7G** and **Supplementary Fig. 6D**). This result suggests that Wnt activity may be responsible for cell proliferation in the CH and ChP region. Supporting this finding, it was shown that ectopic Wnt signaling converts ChP cells into proliferative CH neural cells [7]. Similarly, in the 4th ventricle, two Wnt genes, *Wnt1* and *Wnt3a*, and *mKi67* all became ectopically expressed in *Prdm16* mutant ChP cells (**Supplementary Fig. 7**). Thus, PRDM16 also suppresses Wnt signaling in the hindbrain ChP.

Additionally, six cell-proliferation-related genes (Spc24, Spc25, Nuf2, Ndc80, Id3 and Mybl2) exhibited upregulation in *Prdm16* mutant ChP (**Supplementary Fig. 8**). Interestingly, all four NDC80 complex genes became upregulated, pointing to its potential role in promoting NSC proliferation. Taken together, our results suggest that specification of the ChP epithelium requires a process transitioning proliferating NSCs into quiescence, and that this process is mediated by a suppressive role of PRDM16 on Wnt signaling and cell cycle regulators.

Discussion

In this study we reveal a new molecular mechanism by which BMP signaling regulates cell proliferation and gene expression. We find that PRDM16 acts as a tethering factor to localize the SMAD4/pSMAD1/5/8 complex at specific genomic sites and facilitate the repressive role of the SMAD proteins. The genes co-repressed by PRDM16 and BMP signaling include those encoding Wnt pathway ligands and other cell proliferation regulators.

Combinatory activities of morphogens are exploited throughout animal development and tissue homeostasis. The crosstalk between BMP and WNT signaling is complex as it can be synergistic or antagonistic [42]. Surprisingly, both types of effects exist in the specification of ChP epithelium. Here BMP signaling induces NSC quiescence, as evidenced by the presence of ectopic proliferating cells at the ChP in *Bmpr1a* mutant mice [5], while Wnt signaling promotes proliferation since the gain-of-function condition of beta-Catenin phenocopies *Bmpr1a* mutant animals [7]. On the other hand, adding a low dose of Wnt activator to cell culture medium enhances programing efficiency of ChP epithelial cells induced by BMP4 [43], and loss-of-function of beta-Catenin resulted in under-developed ChP structure [7], suggesting that BMP and WNT signaling collaborate to promote ChP epithelial cell differentiation. Our work demonstrated that PRDM16 ensures the right balance of BMP and Wnt activity by maintaining a low level of Wnt gene expression in the developing ChP.

PRDM16 was shown to physically interact with SMAD3 in *in vitro* assays [18] and antagonize TGF-β induced cell cycle arrest [44]. However, we failed to detect a stable PRDM16/SMAD4/pSMAD1/5/8 or PRDM16/SMAD4/SMAD3 complex in co-immunoprecipitation experiments (data not shown). Instead, our sequential ChIP assay showed that PRDM16 and SMAD4 bind to the same DNA molecule, suggesting that their cooperative activity at the co-bound *cis* regulatory loci. We further identified the intrinsic difference of the DNA sequences bound by SMADs when associated with PRDM16 compared to those without PRDM16, with SMADs preferentially binding to the palindromic motif in the presence of PRDM16 and to the classic GC-rich SBE motifs in the absence of PRDM16. This provides a mechanistic insight into how SMADs switch its regulatory activity from repressing to activating gene expression.

It was shown that PRDM16 antagonized the anti-proliferation activity of TGF-β and SMAD3. However, we show here that PRDM16 collaborates SMAD4 and pSMAD1/5/8 to suppress

proliferation genes, which is consistent with the quiescence-inducing function of BMP signaling. This finding is consistent with those in other developmental contexts such as osteoblast differentiation and maturation where BMP signaling induces differentiation while TGF-β promotes progenitor proliferation [45]. Such functional allocation is likely through regulating distinct sets of target genes. Indeed, in our genomic data, we found that in the cells with high levels of BMP4, PRDM16, pSMAD1/5/8, SMAD4 occupy many more genomic loci, which are excluded from SMAD3 binding, suggesting PRDM16 mainly regulates BMP target genes when there is high BMP signaling.

Moreover, while it was reported that PRDM16 enhances Wnt signaling by stabilizing nuclear beta-Catenin in the craniofacial tissue [21], we detected the opposite outcome in the ChP and cultured NSCs, ectopic WNT gene expression in the absence of *Prdm16*, suggesting that PRDM16 represses Wnt genes in these contexts. Notably, PRDM16, Wnt and BMP co-exist in various developmental settings, such as craniofacial development [16,21,46], heart formation [22,47,48], limb patterning [16,49,50], adult intestinal stem cells [51-53] *etc*. We speculate a similar regulatory circuit is used in some, if not all, of these settings.

ChP epithelial cells derive from proliferating NSCs, without intermediate fate-commitment steps. This property endows ChP cells with higher plasticity and makes them more vulnerable to abnormal genetic and cellular change, to which high occurrence frequency of ChP tumors in fetuses and young children may be attributed [54]. As an essential brain structure, the ChP releases cerebrospinal fluid (CSF) and acts as a brain-blood barrier [55-57]. Its dysfunction has been linked with several types of human diseases including hydrocephalus, Alzheimer's disease, multiple sclerosis [57]. Deepening our knowledge on the development of ChP will provide new insights into potential therapeutics to prevent or treat ChP tumors and other ChP-related diseases.

Footnote: a study on the antagonism between PRDM16 and SMAD4 was published on Feb 24, 2023 (Hurwitz, 2023) after we posted our manuscript at BioRxiv and during our submission process.

Materials and methods

Animals

All animal procedures were approved by Swedish agriculture board (Jordbruks Verket) with document number Dnr 11553-2017 and 11766-2022. The *Prdm16*^{cGT} mice [17] were maintained by outcrossing with the FVB/NJ line.

In situ hybridization:

To make probes for conventional RNA in situ hybridization, genomic regions covering one exon or full-length cDNA were PCR amplified to generate fragments with restriction enzyme overhangs. The sequences of all oligos were included in Supplementary table 1. The fragments were inserted to the pBluescript SK(II) vector. In vitro transcription was performed as previously described (He et al., 2021). The mouse brains at defined ages were dissected and fixed for 12 hours in 4% PFA, dehydrated in 25% sucrose, cryoprotected and embedded in O.C.T. The brain samples were then sectioned at 18 μm thickness on Leica cryostats CM3050s. RNA *in situ* hybridization was performed using digoxigenin-labeled riboprobes as described previously. Detailed protocols are available upon request. Images were taken using a Leica DMLB microscope.

Immunostaining

Immunostaining was performed according to standard protocols as previously used [58]. For EdU and BrdU labeling, EdU (5-ethynyl-2′-deoxyuridine) and BrdU (5-bromo-2'-deoxyuridine) (5-20 μg/g of body weight) were injected into the peritoneal cavity of pregnant mice at desired ages. EdU incorporation was detected with the Click-iT assay (Invitrogen) according to the manufacturer's instructions. BrdU incorporation was measured by immunostaining using an antibody against rat-BrdU (Abcam). Imaging was taken on a Zeiss confocal microscope. ZEN (ZeissLSM800), ImageJ (NIH) and Photoshop (Adobe) were used for analysis and quantification.

NSC culture

Control and mutant embryonic cortices from E13.5 animals were dissected and dissociated into single cell suspension and digested with Accutase (Sigma). Cells were maintained in

proliferation media (STEMCELL Technologies). Lentivirus expressing Flag-*Prdm16* and a puromycin resistant gene in the pCDH vector was produced in 293J4 cells and used to infect a wild-type NSC line derived from E13.5 forebrain, and the selected NSCs were maintained in puromycin-containing medium for three passages before puromycin withdrawal.

RT-qPCR

Prdm16_Expressing, wild-type and mutant NSCs were cultured and treated with or without BMP4 (Sigma). After 48-hour treatment, total RNAs were extracted using TRIzol reagent (Invitrogen). Total RNA was further cleaned with Turbo DNase (Ambion) and used in reverse-transcription with RT master mix (ThermoFisher). To ensure the absence of genomic DNA, control qPCR was performed on the mock-reverse-transcribed RNA samples. The list of qPCR primers is included in supplementary table 1.

SCRINSHOT

Brain sections were prepared in the same way as for regular *in situ* hybridization (described above). The SCRINSHOT experiments were carried out according to the published method [41]. In brief, 3 padlock probes and 3 corresponding detection probes were designed for each gene of interest. The slides with cryo-sectioned brain slices were pretreated at 45˚C to reduce moisture and fixed in 4% PFA in 1X PBS, followed by washing in PBS Tween-20 0.05% twice. Permeabilization of tissues were done by washing slides in 0.1M HCl for 2mins 15s, followed by washing in PBS Tween-20 0.05% twice. Then a stepwise dehydration was performed for the slides in 70%, 85% & 100% Ethanol and air. The SecureSeal hybridization chamber (GRACE BIO-LABS, 621501) was then mounted to cover each pair of control and *Prdm16* mutant brain slices. Samples were then blocked in a probe-free hybridization reaction mixture of 1XAmplifase buffer (Lucigen, A1905B), 0.05M KCl, 20% Formamide deionized (Millipore S4117), 0.1uM Oligo-dT, 0.1ug/ul BSA (New England Biolabs, B9000S), 1U/ul RiboLock (Thermo, EO0384), and 0.2ug/ul tRNAs (Ambion, AM7119). Then hybridization of padlock probes was done by incubating samples with padlock probes (with the concentration of each one 0.01uM) mixed in blocking reagents used before (no oligo dT used in this step). The slide was then put into a PCR machine to denature at 55˚C for 15 minutes and hybridize at 45˚C for 120 minutes. Padlock probes were then ligated by using SplintR ligase (NEB M0375) at 25˚C for 16 hours followed by RCA (rolling cycle amplification) at 30˚C for 16 hours by using phi29 polymerase (Lucigen, 30221–2) and RCA primer1. Then a fixation step was applied to stabilize

RCA product in 4% PFA for 15 minutes followed by washing in PBS Tween-20 0.05%. Then the hybridization of the first 3 genes was done by mixing all 3 3' fluorophore-conjugated detection probes of each gene in reaction reagent (2XSSC, 20% Formamide deionized, 0.1ug/ul BSA, and 0.5 ng/µl DAPI (Biolegend, 422801) followed by hybridization at 30˚C for 1 hour. The slides were washed in 20% formamide in 2X SSC and then in 6X SSC, followed by dehydration in 70%, 85%, 100% Ethanol until the chamber was removed. Then the samples were preserved in SlowFade Gold Antifade mountant (Thermo, S36936) and kept in dark before imaging. After image acquisition, the first 3 detection probes were removed by using Uracil-DNA Glycosylase (Thermo, EN0362), and the slides were ready for the next round of detection probe hybridization. The procedure was repeated until all genes were hybridized and imaged.

Images were acquired with Zeiss Axio Observer 7 fluorescent microscope with an automated stage setting to fix imaging region for different hybridization rounds. Image analysis was done according to the published method [41]. In brief, the DAPI channel from each round was extracted to measure the shift of imaging. The images were then aligned for all gene channels in Zen by Creating Image Subset with the shifting value. After alignment, images were exported into TIFF files and the threshold analysis was carried out for individual channel one by one in CellProfiler with scripts provided by the published method (Alexandros et al. 2020). Then nuclear segmentation was done manually in Fiji ROI manager to obtain nuclear ROIs, followed by an expansion of 2 um in CellProfiler to obtain cell ROIs. Then signal dots were count in these cell ROIs for each gene in CellProfiler and Fiji. Summary of the dot counts for each gene was exported to Excel files.

CUT&TAG

CUT&TAG was performed according to the published method [59]. In brief, *Prdm16*_E and *Prdm16* mutant NSCs were cultured in NeuroCult™ Proliferation Kit (Stem cell technologies, 05702) for 3 days with or without BMP4 at concentration of 25ng/ml medium (Sigma, H4916). Cells on day 3 were then shortly rinsed with 1X PBS and resuspended in 1ml cold NE1 buffer on ice. Nuclei were lightly fixed with 0.1% formaldehyde to 1ml PBS at RT for 2 minutes and neutralized with 75mM Glycine. Nuclei were then washed for 3 times, resuspended in 1mL wash buffer and mixed with 90uL Concanavalin A-coated magnetic beads (Polyscience 86057). The nuclei/beads mix was then blocked with 800 uL cold Antibody buffer for 5 minutes and resuspended in 1.2 mL Antibody buffer and aliquoted into 8 tubes with 150 uL each. 2 uL Anti-PRDM16 (Generous gift from Bryan Bjork lab) or IgG (SIGMA-ALDRICH, I5006) was added

into each tube for an overnight incubation at 4°C. The beads/nuclei/antibody mix was then washed with Dig-wash buffer and incubated with secondary antibody (1:100 dilution) for 1 hour. After further washes with the Dig-wash buffer. a pA-Tn5 adaptor complex in Dig-300 buffer was added to the beads for 1 hour reaction. The beads were then washed with Dig-300 buffer before the incubation with 300ul Tagmentation buffer at 37°C for 1 hour. Then 10ul 0.5M EDTA, 3uL 10% SDS and 2.5uL 20 mg/mL proteinase K (Invitrogen) were used to stop the reaction. Then the resultant DNA was purified with DNA clean & Concentrator kit (ZYMO Research D4013) and eluted in 25uL Elution buffer. To generate libraries, 21uL fragment DNA was mixed with 2uL 10uM Universal i5 primer, 2uL 10uM uniquely barcoded i7 primer and 25uL PCR master mix (NEB Phusion® High-Fidelity PCR Master Mix with HF Buffer, M0531). The PCR condition was as follows: 72°C 5min, 98°C 30s, repeat 12 times (98°C 10s, 63°C 10s), 72°C 1 min and hold 4°C. The libraries were cleaned with standard Ampure XP beads as previously described. Libraries from four biological replicates were produced for each condition.

ChIP

ChIP was performed as previously described [60]. For each ChIP reaction, 10 million Prdm16_E, Prdm16_KO NSCs with or without 3-day BMP4 treatment were fixed, lysed, sonicated and made into chromatin extract. After precleared with gamma-bind-G beads, the chromatin extract was incubated with 2ug PRDM16, 2ug SMAD4 (Proteintech, 10231-1-AP), 2ug pSMAD1/5/8 (Millipore, AB3848-1) or 2ug SMAD3 (abcam, ab227223) in each ChIP reaction. In sequential ChIP assays, the same chromatin lysate was precleared and used, but with more antibodies in each reaction: 5 ug of IgG or PRDM16 antibody in the first round of immunoprecipitation. The elutes were then precleared again using gamma-bind G beads, divided into two equal halves and immunoprecipitated with 2 ug of IgG or the SMAD4 antibody. In ChIP-qPCR experiments, 2ug SMAD4 and 2 ug c-FOS antibodies (Invitrogen, MA5-15055) were used in each reaction. The precipitated DNA was reverse cross-linked, and then purified using the Qiagen PCR purification kit.

Computation analyses

ChIP-seq libraries and analyses. 0.2% input and ChIPed DNA were made into libraries using the NEBNext Ultra™ II DNA Library Prep Kit and sequenced on the Illumina Nextseq500 platform. Three replicates of ChIP-seq samples, after the adaptor trimming by Trimmomatic,

were mapped to the UCSC *Mus musculus* (mm10) genome assembly using Bowtie2 with the default parameters. The uniquely mapped reads (with mapping quality >= 20) were used for further analyses. The peaks were called by HOMER (v4.10) [61]. The reproducibility between replicates was estimated by Irreproducibility Discovery Rate (IDR), using the HOMER IDR pipeline (https://github.com/karmel/homer-idr). As suggested by the Encode IDR guideline, we used a relatively relaxed parameter "-F 2 -fdr 0.3 -P .1 -L 3 -LP .1" for the true/pseudo/pooled replicates by the HOMER peak calling. The final confident peaks were determined by an IDR < 5%. The peaks that were overlapped with mm10 blacklist were also removed.

CUT&TAG analyses. The CUT&TAG samples of Prdm16_E and Prdm16 mutant NSCs in four replicates, and of Prdm16 from CH and ChP area at stage 12.5 embryos in three replicates, were mapped to mm10 genome assembly using Bowtie2 (bowtie2 --end-to-end --very-sensitive --no-mixed --no-discordant --phred33 -I 10 -X 700). The CUT&TAG coverage for these samples were generated by bedtools genomeCoverageBed and normalized to the library depths to give a read per million per base (RPM). By using the peak caller SEACR [29], which was designed for calling peaks from sparse chromatin profiling data such as CUT&TAG [22], we performed peak calling with FDR < 10% for each replicated sample (SEACR_1.3.sh normalized_coverage 0.1 non stringent output_peaks). To identify confident peaks, we selected the common peaks, which were called from all replicates for each condition. Peak overlapping analysis was performed by Homer mergePeaks function with default parameters. Peak overlap analysis utilized HOMER's mergePeaks function, specifically employing the default '-d given' parameter. This approach ensures that only peaks directly overlapping with each other are merged, maintaining the precise distances between peaks as provided in the input peak calls. This method is particularly beneficial for retaining the integrity of the original peak boundaries, avoiding any alterations to their relative positions. *De novo* motif discovery from SMAD4 and pSMAD1/5/8 peaks in Prdm16_E NSCs and Prdm16 mutant NSCs were performed by MEME-ChIP software [62] (parameters: -ccut 100 -meme-p 5 -dna -meme-mod anr -minw 5 -maxw 15 -filter-thresh 0.05).

The CUT&TAG samples of H3K4me3 BMP4-treated and non-treated *Prdm16*_E and *Prdm16*_KO cells in 2 or 3 replicates were mapped to mm10 genome assembly using Bowtie2 (bowtie2 --end-to-end --very-sensitive --no-mixed --no-discordant --phred33 -I 10 -X 700). Differential analysis of TSS up-stream and down-stream 500 bp between Prdm16_E BMP-treated vs non-BMP-treated and Prdm16_KO vs Prdm16_E BMP-treated were performed by

Limma R package [63]. Gene Ontology (GO) enrichment analysis of up-regulated and down-regulated regions was performed by PANTHER [64].

scRNA-seq analyses. The scRNA-seq data of the developing mouse brain were obtained from [37]. The counts per cell were normalized by logNormCounts function in Bioconductor package "scater" and the normalized expression data per cell were used to generate gene expression violin plots. To test whether Prdm16 target gene sets of Prdm16 with and without BMP4 and ChP E12.5 are significantly enriched among the scRNA-seq gene mean expression in each identified cell type cluster, the gene set enrichment analysis (GESA) "fgesa" Bioconductor package was used [ref: Korotkevich G. et al. Fast gene set enrichment analysis. bioRxiv, 2021. http://biorxiv.org/content/early/2016/06/20/060012].

Acknowledgements

We thank the animal experimental core facility and the imaging facility of Stockholm University and Bioinformatics and Expression analysis core facility at Karolinska Institute, Sweden, for their service and support. We thank Christos Samakovlis and his lab members for technical help on SCRINSHOT experiments. We also appreciate technical help from Adrian Martinez Martin. J.W. is funded by Australian Research Council Centre of Excellence for the Mathematical Analysis of Cellular Systems (CE230100001) and ANU Future Scheme. The project was supported by the research project grant from Swedish Research Council (Vetenskapsrådet, 2020-03543) and the research grants from Swedish Cancerfonden (CAN 2017/529 and 20 1046 PjF 01 H) to Q.D.

Author contributions

Q.D. conceived and designed the project. L.H. performed all of the experiments. J.W performed all computational analysis. Q.D., J.W. and L.H. analysed and interpreted the data. Q.D. wrote the manuscript with input from L.H. and J.W.

Data availability: The CUT&TAG and ChIP-seq data produced in this study have been deposited to Gene Expression Omnibus (GEO accession number: GSE275758).

Reference:

1. Zhang, J., and Li, L. (2005). BMP signaling and stem cell regulation. Dev Biol *284*, 1-11. 10.1016/j.ydbio.2005.05.009.
2. Martin-Malpartida, P., Batet, M., Kaczmarska, Z., Freier, R., Gomes, T., Aragon, E., Zou, Y., Wang, Q., Xi, Q., Ruiz, L., et al. (2017). Structural basis for genome wide recognition of 5-bp GC motifs by SMAD transcription factors. Nat Commun *8*, 2070. 10.1038/s41467-017-02054-6.
3. Hill, C.S. (2016). Transcriptional Control by the SMADs. Cold Spring Harb Perspect Biol *8*. 10.1101/cshperspect.a022079.
4. Liddelow, S.A., Dziegielewska, K.M., Vandeberg, J.L., and Saunders, N.R. (2010). Development of the lateral ventricular choroid plexus in a marsupial, Monodelphis domestica. Cerebrospinal Fluid Res *7*, 16. 10.1186/1743-8454-7-16.
5. Hebert, J.M., Mishina, Y., and McConnell, S.K. (2002). BMP signaling is required locally to pattern the dorsal telencephalic midline. Neuron *35*, 1029-1041. 10.1016/s0896-6273(02)00900-5.
6. Watanabe, M., Kang, Y.J., Davies, L.M., Meghpara, S., Lau, K., Chung, C.Y., Kathiriya, J., Hadjantonakis, A.K., and Monuki, E.S. (2012). BMP4 sufficiency to induce choroid plexus epithelial fate from embryonic stem cell-derived neuroepithelial progenitors. J Neurosci *32*, 15934-15945. 10.1523/JNEUROSCI.3227-12.2012.
7. Parichha, A., Suresh, V., Chatterjee, M., Kshirsagar, A., Ben-Reuven, L., Olender, T., Taketo, M.M., Radosevic, V., Bobic-Rasonja, M., Trnski, S., et al. (2022). Constitutive activation of canonical Wnt signaling disrupts choroid plexus epithelial fate. Nat Commun *13*, 633. 10.1038/s41467-021-27602-z.
8. Aguilo, F., Avagyan, S., Labar, A., Sevilla, A., Lee, D.F., Kumar, P., Lemischka, I.R., Zhou, B.Y., and Snoeck, H.W. (2011). Prdm16 is a physiologic regulator of hematopoietic stem cells. Blood *117*, 5057-5066. 10.1182/blood-2010-08-300145.
9. Chuikov, S., Levi, B.P., Smith, M.L., and Morrison, S.J. (2010). Prdm16 promotes stem cell maintenance in multiple tissues, partly by regulating oxidative stress. Nat Cell Biol *12*, 999-1006. 10.1038/ncb2101.
10. Kajimura, S., Seale, P., Tomaru, T., Erdjument-Bromage, H., Cooper, M.P., Ruas, J.L., Chin, S., Tempst, P., Lazar, M.A., and Spiegelman, B.M. (2008). Regulation of the brown and white fat gene programs through a PRDM16/CtBP transcriptional complex. Genes & development *22*, 1397-1409. 10.1101/gad.1666108.
11. Shimada, I.S., Acar, M., Burgess, R.J., Zhao, Z., and Morrison, S.J. (2017). Prdm16 is required for the maintenance of neural stem cells in the postnatal forebrain and their differentiation into ependymal cells. Genes & development *31*, 1134-1146. 10.1101/gad.291773.116.
12. Chui, A., Zhang, Q., Dai, Q., and Shi, S.H. (2020). Oxidative stress regulates progenitor behavior and cortical neurogenesis. Development *147*. 10.1242/dev.184150.
13. Baizabal, J.M., Mistry, M., Garcia, M.T., Gomez, N., Olukoya, O., Tran, D., Johnson, M.B., Walsh, C.A., and Harwell, C.C. (2018). The Epigenetic State of PRDM16-Regulated Enhancers in Radial Glia Controls Cortical Neuron Position. Neuron *98*, 945-962 e948. 10.1016/j.neuron.2018.04.033.
14. Inoue, M., Iwai, R., Tabata, H., Konno, D., Komabayashi-Suzuki, M., Watanabe, C., Iwanari, H., Mochizuki, Y., Hamakubo, T., Matsuzaki, F., et al. (2017). Prdm16 is

759 crucial for progression of the multipolar phase during neural differentiation of the
760 developing neocortex. Development *144*, 385-399. 10.1242/dev.136382.
761 15. He, L., Jones, J., He, W., Bjork, B.C., Wen, J., and Dai, Q. (2021). PRDM16 regulates a
762 temporal transcriptional program to promote progression of cortical neural
763 progenitors. Development *148*. 10.1242/dev.194670.
764 16. Bjork, B.C., Turbe-Doan, A., Prysak, M., Herron, B.J., and Beier, D.R. (2010). Prdm16 is
765 required for normal palatogenesis in mice. Hum Mol Genet *19*, 774-789.
766 10.1093/hmg/ddp543.
767 17. Strassman, A., Schnutgen, F., Dai, Q., Jones, J.C., Gomez, A.C., Pitstick, L., Holton,
768 N.E., Moskal, R., Leslie, E.R., von Melchner, H., et al. (2017). Generation of a
769 multipurpose Prdm16 mouse allele by targeted gene trapping. Dis Model Mech *10*,
770 909-922. 10.1242/dmm.029561.
771 18. Warner, D.R., Horn, K.H., Mudd, L., Webb, C.L., Greene, R.M., and Pisano, M.M.
772 (2007). PRDM16/MEL1: a novel Smad binding protein expressed in murine embryonic
773 orofacial tissue. Biochim Biophys Acta *1773*, 814-820. 10.1016/j.bbamcr.2007.03.016.
774 19. Seale, P., Kajimura, S., Yang, W., Chin, S., Rohas, L.M., Uldry, M., Tavernier, G., Langin,
775 D., and Spiegelman, B.M. (2007). Transcriptional control of brown fat determination
776 by PRDM16. Cell Metab *6*, 38-54. 10.1016/j.cmet.2007.06.001.
777 20. Tseng, Y.H., Kokkotou, E., Schulz, T.J., Huang, T.L., Winnay, J.N., Taniguchi, C.M., Tran,
778 T.T., Suzuki, R., Espinoza, D.O., Yamamoto, Y., et al. (2008). New role of bone
779 morphogenetic protein 7 in brown adipogenesis and energy expenditure. Nature
780 *454*, 1000-1004. 10.1038/nature07221.
781 21. Shull, L.C., Lencer, E.S., Kim, H.M., Goyama, S., Kurokawa, M., Costello, J.C., Jones, K.,
782 and Artinger, K.B. (2022). PRDM paralogs antagonistically balance Wnt/beta-catenin
783 activity during craniofacial chondrocyte differentiation. Development *149*.
784 10.1242/dev.200082.
785 22. Arndt, A.K., Schafer, S., Drenckhahn, J.D., Sabeh, M.K., Plovie, E.R., Caliebe, A.,
786 Klopocki, E., Musso, G., Werdich, A.A., Kalwa, H., et al. (2013). Fine mapping of the
787 1p36 deletion syndrome identifies mutation of PRDM16 as a cause of
788 cardiomyopathy. Am J Hum Genet *93*, 67-77. 10.1016/j.ajhg.2013.05.015.
789 23. Mira, H., Andreu, Z., Suh, H., Lie, D.C., Jessberger, S., Consiglio, A., San Emeterio, J.,
790 Hortiguela, R., Marques-Torrejon, M.A., Nakashima, K., et al. (2010). Signaling
791 through BMPR-IA regulates quiescence and long-term activity of neural stem cells in
792 the adult hippocampus. Cell Stem Cell *7*, 78-89. 10.1016/j.stem.2010.04.016.
793 24. Hu, J.S., Doan, L.T., Currle, D.S., Paff, M., Rheem, J.Y., Schreyer, R., Robert, B., and
794 Monuki, E.S. (2008). Border formation in a Bmp gradient reduced to single
795 dissociated cells. Proc Natl Acad Sci U S A *105*, 3398-3403.
796 10.1073/pnas.0709100105.
797 25. Wang, Q., Li, H., Tajima, K., Verkerke, A.R.P., Taxin, Z.H., Hou, Z., Cole, J.B., Li, F.,
798 Wong, J., Abe, I., et al. (2022). Post-translational control of beige fat biogenesis by
799 PRDM16 stabilization. Nature *609*, 151-158. 10.1038/s41586-022-05067-4.
800 26. Benayoun, B.A., Pollina, E.A., Ucar, D., Mahmoudi, S., Karra, K., Wong, E.D.,
801 Devarajan, K., Daugherty, A.C., Kundaje, A.B., Mancini, E., et al. (2014). H3K4me3
802 breadth is linked to cell identity and transcriptional consistency. Cell *158*, 673-688.
803 10.1016/j.cell.2014.06.027.
804 27. Katada, S., Takouda, J., Nakagawa, T., Honda, M., Igarashi, K., Imamura, T., Ohkawa,
805 Y., Sato, S., Kurumizaka, H., and Nakashima, K. (2021). Neural stem/precursor cells

806 dynamically change their epigenetic landscape to differentially respond to BMP
807 signaling for fate switching during brain development. Genes & development *35*,
808 1431-1444. 10.1101/gad.348797.121.
809 28. Tooley, J., and Stukenberg, P.T. (2011). The Ndc80 complex: integrating the
810 kinetochore's many movements. Chromosome Res *19*, 377-391. 10.1007/s10577-
811 010-9180-5.
812 29. Meers, M.P., Tenenbaum, D., and Henikoff, S. (2019). Peak calling by Sparse
813 Enrichment Analysis for CUT&RUN chromatin profiling. Epigenetics Chromatin *12*, 42.
814 10.1186/s13072-019-0287-4.
815 30. Zawel, L., Dai, J.L., Buckhaults, P., Zhou, S., Kinzler, K.W., Vogelstein, B., and Kern, S.E.
816 (1998). Human Smad3 and Smad4 are sequence-specific transcription activators. Mol
817 Cell *1*, 611-617. 10.1016/s1097-2765(00)80061-1.
818 31. Dennler, S., Itoh, S., Vivien, D., ten Dijke, P., Huet, S., and Gauthier, J.M. (1998).
819 Direct binding of Smad3 and Smad4 to critical TGF beta-inducible elements in the
820 promoter of human plasminogen activator inhibitor-type 1 gene. EMBO J *17*, 3091-
821 3100. 10.1093/emboj/17.11.3091.
822 32. Wong, C., Rougier-Chapman, E.M., Frederick, J.P., Datto, M.B., Liberati, N.T., Li, J.M.,
823 and Wang, X.F. (1999). Smad3-Smad4 and AP-1 complexes synergize in
824 transcriptional activation of the c-Jun promoter by transforming growth factor beta.
825 Mol Cell Biol *19*, 1821-1830. 10.1128/MCB.19.3.1821.
826 33. Pyrowolakis, G., Hartmann, B., Muller, B., Basler, K., and Affolter, M. (2004). A simple
827 molecular complex mediates widespread BMP-induced repression during Drosophila
828 development. Dev Cell *7*, 229-240. 10.1016/j.devcel.2004.07.008.
829 34. Gao, S., Steffen, J., and Laughon, A. (2005). Dpp-responsive silencers are bound by a
830 trimeric Mad-Medea complex. J Biol Chem *280*, 36158-36164.
831 10.1074/jbc.M506882200.
832 35. Weiss, A., Charbonnier, E., Ellertsdottir, E., Tsirigos, A., Wolf, C., Schuh, R.,
833 Pyrowolakis, G., and Affolter, M. (2010). A conserved activation element in BMP
834 signaling during Drosophila development. Nat Struct Mol Biol *17*, 69-76.
835 10.1038/nsmb.1715.
836 36. Zhang, Y., Feng, X.H., and Derynck, R. (1998). Smad3 and Smad4 cooperate with c-
837 Jun/c-Fos to mediate TGF-beta-induced transcription. Nature *394*, 909-913.
838 10.1038/29814.
839 37. La Manno, G., Siletti, K., Furlan, A., Gyllborg, D., Vinsland, E., Mossi Albiach, A.,
840 Mattsson Langseth, C., Khven, I., Lederer, A.R., Dratva, L.M., et al. (2021). Molecular
841 architecture of the developing mouse brain. Nature *596*, 92-96. 10.1038/s41586-021-
842 03775-x.
843 38. Rhodes, C.T., Thompson, J.J., Mitra, A., Asokumar, D., Lee, D.R., Lee, D.J., Zhang, Y.,
844 Jason, E., Dale, R.K., Rocha, P.P., and Petros, T.J. (2022). An epigenome atlas of neural
845 progenitors within the embryonic mouse forebrain. Nat Commun *13*, 4196.
846 10.1038/s41467-022-31793-4.
847 39. Kalani, M.Y., Cheshier, S.H., Cord, B.J., Bababeygy, S.R., Vogel, H., Weissman, I.L.,
848 Palmer, T.D., and Nusse, R. (2008). Wnt-mediated self-renewal of neural
849 stem/progenitor cells. Proc Natl Acad Sci U S A *105*, 16970-16975.
850 10.1073/pnas.0808616105.
851 40. Harrison-Uy, S.J., and Pleasure, S.J. (2012). Wnt signaling and forebrain development.
852 Cold Spring Harb Perspect Biol *4*, a008094. 10.1101/cshperspect.a008094.

853 41. Sountoulidis, A., Liontos, A., Nguyen, H.P., Firsova, A.B., Fysikopoulos, A., Qian, X.,
854 Seeger, W., Sundstrom, E., Nilsson, M., and Samakovlis, C. (2020). SCRINSHOT
855 enables spatial mapping of cell states in tissue sections with single-cell resolution.
856 PLoS Biol *18*, e3000675. 10.1371/journal.pbio.3000675.
857 42. Itasaki, N., and Hoppler, S. (2010). Crosstalk between Wnt and bone morphogenic
858 protein signaling: a turbulent relationship. Dev Dyn *239*, 16-33. 10.1002/dvdy.22009.
859 43. Pellegrini, L., Bonfio, C., Chadwick, J., Begum, F., Skehel, M., and Lancaster, M.A.
860 (2020). Human CNS barrier-forming organoids with cerebrospinal fluid production.
861 Science *369*. 10.1126/science.aaz5626.
862 44. Takahata, M., Inoue, Y., Tsuda, H., Imoto, I., Koinuma, D., Hayashi, M., Ichikura, T.,
863 Yamori, T., Nagasaki, K., Yoshida, M., et al. (2009). SKI and MEL1 cooperate to inhibit
864 transforming growth factor-beta signal in gastric cancer cells. J Biol Chem *284*, 3334-
865 3344. 10.1074/jbc.M808989200.
866 45. Wu, M., Chen, G., and Li, Y.P. (2016). TGF-beta and BMP signaling in osteoblast,
867 skeletal development, and bone formation, homeostasis and disease. Bone Res *4*,
868 16009. 10.1038/boneres.2016.9.
869 46. Nie, X., Luukko, K., and Kettunen, P. (2006). BMP signalling in craniofacial
870 development. Int J Dev Biol *50*, 511-521. 10.1387/ijdb.052101xn.
871 47. van Wijk, B., Moorman, A.F., and van den Hoff, M.J. (2007). Role of bone
872 morphogenetic proteins in cardiac differentiation. Cardiovasc Res *74*, 244-255.
873 10.1016/j.cardiores.2006.11.022.
874 48. Gessert, S., and Kuhl, M. (2010). The multiple phases and faces of wnt signaling
875 during cardiac differentiation and development. Circ Res *107*, 186-199.
876 10.1161/CIRCRESAHA.110.221531.
877 49. Geetha-Loganathan, P., Nimmagadda, S., and Scaal, M. (2008). Wnt signaling in limb
878 organogenesis. Organogenesis *4*, 109-115. 10.4161/org.4.2.5857.
879 50. Robert, B. (2007). Bone morphogenetic protein signaling in limb outgrowth and
880 patterning. Dev Growth Differ *49*, 455-468. 10.1111/j.1440-169X.2007.00946.x.
881 51. Stine, R.R., Sakers, A.P., TeSlaa, T., Kissig, M., Stine, Z.E., Kwon, C.W., Cheng, L., Lim,
882 H.W., Kaestner, K.H., Rabinowitz, J.D., and Seale, P. (2019). PRDM16 Maintains
883 Homeostasis of the Intestinal Epithelium by Controlling Region-Specific Metabolism.
884 Cell Stem Cell *25*, 830-845 e838. 10.1016/j.stem.2019.08.017.
885 52. Korinek, V., Barker, N., Moerer, P., van Donselaar, E., Huls, G., Peters, P.J., and
886 Clevers, H. (1998). Depletion of epithelial stem-cell compartments in the small
887 intestine of mice lacking Tcf-4. Nat Genet *19*, 379-383. 10.1038/1270.
888 53. He, X.C., Zhang, J., Tong, W.G., Tawfik, O., Ross, J., Scoville, D.H., Tian, Q., Zeng, X.,
889 He, X., Wiedemann, L.M., et al. (2004). BMP signaling inhibits intestinal stem cell self-
890 renewal through suppression of Wnt-beta-catenin signaling. Nat Genet *36*, 1117-
891 1121. 10.1038/ng1430.
892 54. Wolff, J.E., Sajedi, M., Brant, R., Coppes, M.J., and Egeler, R.M. (2002). Choroid plexus
893 tumours. Br J Cancer *87*, 1086-1091. 10.1038/sj.bjc.6600609.
894 55. Johansson, P.A. (2014). The choroid plexuses and their impact on developmental
895 neurogenesis. Front Neurosci *8*, 340. 10.3389/fnins.2014.00340.
896 56. Lehtinen, M.K., Bjornsson, C.S., Dymecki, S.M., Gilbertson, R.J., Holtzman, D.M., and
897 Monuki, E.S. (2013). The choroid plexus and cerebrospinal fluid: emerging roles in
898 development, disease, and therapy. J Neurosci *33*, 17553-17559.
899 10.1523/JNEUROSCI.3258-13.2013.

57. Lun, M.P., Monuki, E.S., and Lehtinen, M.K. (2015). Development and functions of the choroid plexus-cerebrospinal fluid system. Nat Rev Neurosci *16*, 445-457. 10.1038/nrn3921.
58. Dai, Q., Andreu-Agullo, C., Insolera, R., Wong, L.C., Shi, S.H., and Lai, E.C. (2013). BEND6 is a nuclear antagonist of Notch signaling during self-renewal of neural stem cells. Development *140*, 1892-1902. 10.1242/dev.087502.
59. Kaya-Okur, H.S., Wu, S.J., Codomo, C.A., Pledger, E.S., Bryson, T.D., Henikoff, J.G., Ahmad, K., and Henikoff, S. (2019). CUT&Tag for efficient epigenomic profiling of small samples and single cells. Nat Commun *10*, 1930. 10.1038/s41467-019-09982-5.
60. Dai, Q., Ren, A., Westholm, J.O., Serganov, A.A., Patel, D.J., and Lai, E.C. (2013). The BEN domain is a novel sequence-specific DNA-binding domain conserved in neural transcriptional repressors. Genes & development *27*, 602-614. 10.1101/gad.213314.113.
61. Heinz, S., Benner, C., Spann, N., Bertolino, E., Lin, Y.C., Laslo, P., Cheng, J.X., Murre, C., Singh, H., and Glass, C.K. (2010). Simple combinations of lineage-determining transcription factors prime cis-regulatory elements required for macrophage and B cell identities. Mol Cell *38*, 576-589. 10.1016/j.molcel.2010.05.004.
62. Machanick, P., and Bailey, T.L. (2011). MEME-ChIP: motif analysis of large DNA datasets. Bioinformatics *27*, 1696-1697. 10.1093/bioinformatics/btr189.
63. Ritchie, M.E., Phipson, B., Wu, D., Hu, Y., Law, C.W., Shi, W., and Smyth, G.K. (2015). limma powers differential expression analyses for RNA-sequencing and microarray studies. Nucleic Acids Res *43*, e47. 10.1093/nar/gkv007.
64. Thomas, P.D., Ebert, D., Muruganujan, A., Mushayahama, T., Albou, L.P., and Mi, H. (2022). PANTHER: Making genome-scale phylogenetics accessible to all. Protein Sci *31*, 8-22. 10.1002/pro.4218.

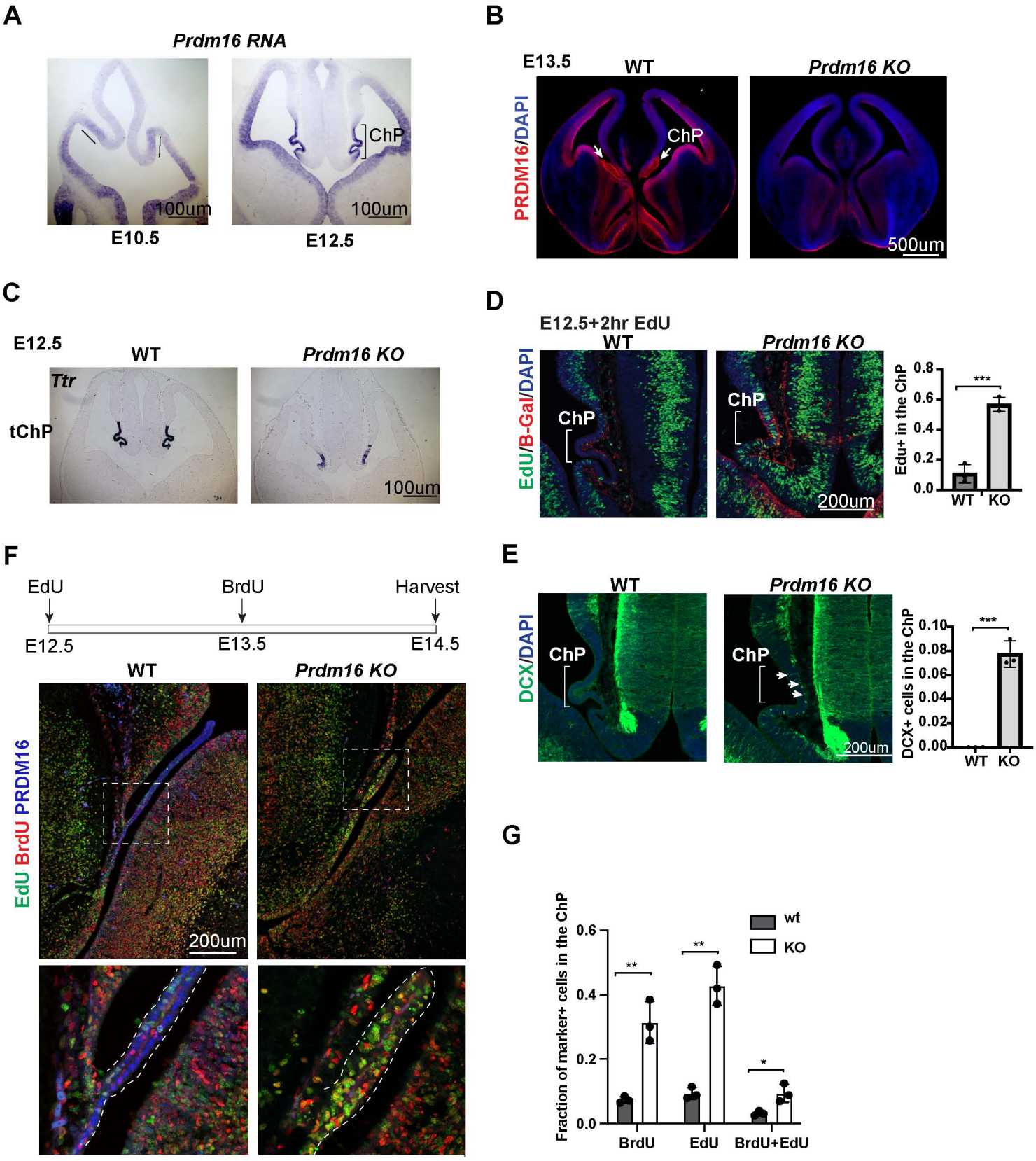
A
Prdm16 RNA
ChP
100um
100um
E10.5
E12.5
B
E13.5
WT
Prdm16 KO
PRDM16/DAPI
ChP
500um
C
E12.5
WT
Prdm16 KO
Ttr
tChP
100um
D
E12.5+2hr EdU
WT
Prdm16 KO
EdU/B-Gal/DAPI
ChP
ChP
200um
Edu+ in the ChP
0.8
0.6
0.4
0.2
0.0
***
WT
KO
E
WT
Prdm16 KO
DCX/DAPI
ChP
ChP
200um
DCX+ cells in the ChP
0.10
0.08
0.06
0.04
0.02
0.00
***
WT
KO
F
EdU
BrdU
Harvest
E12.5
E13.5
E14.5
WT
Prdm16 KO
EdU BrdU PRDM16
200um
G
Fraction of marker+ cells in the ChP
0.6
0.4
0.2
0.0
wt
KO
**
**
*
BrdU
EdU
BrdU+EdU

Figure 1. *Prdm16* mutant ChP cells fail to exit cell cycle and are still neural progenitors

(**A**) RNA *in situ* hybridization with a *Prdm16* probe, showing expression of *Prdm16* in the E10.5 and E12.5 brains. The line and bracket indicate the developing ChP. (**B**) Staining of PRDM16 using a PRDM16 antibody on the E13.5 control and null mutant brains. Red: PRDM16; blue: the nucleus dye DAPI. White arrows indicate the ChP in the control. (**C**) RNA in situ hybridization using a *Ttr* probe on E12.5 control and *Prdm16* null mutant forebrains. (**D**) Two-hour EdU labeling in the E12.5 control and homozygous brains. The brain sections are co-stained with an antibody against B-gal. Note: the lacZ gene trap is present in the heterozygous and homozygous mutants but not in wild-type animals, and the highest expression of B-Gal is seen at the ChP indicated by brackets. Red: B-Gal; blue: the nucleus dye DAPI; green: EdU. (**E**) DCX antibody staining on the E12.5 control and homozygous brain slices. White arrows indicate some of the DCX positive cells. Quantification of EdU+ (**D**) or DCX+ (**E**) cells is shown on the right. Biological replicates: N=3. Error bars represent standard deviation (SD). Statistical significance is calculated using unpaired t-test. ***, $p<0.001$. (**F**) Double S-phase labeling as illustrated on the top. Immunostaining of the control and *Prdm16* KO brain slices using a PRDM16 and a BrdU antibodies and the EdU detection kit. An enlarged view highlight the ChP area is presented below. (**G**) Quantification of EdU+ and BrdU+ cells from the double labeling experiment. Biological replicates: N=3. Error bars represent standard deviation (SD). Statistical significance is calculated using unpaired t-test. ***, $p<0.001$.

He_Figure 2

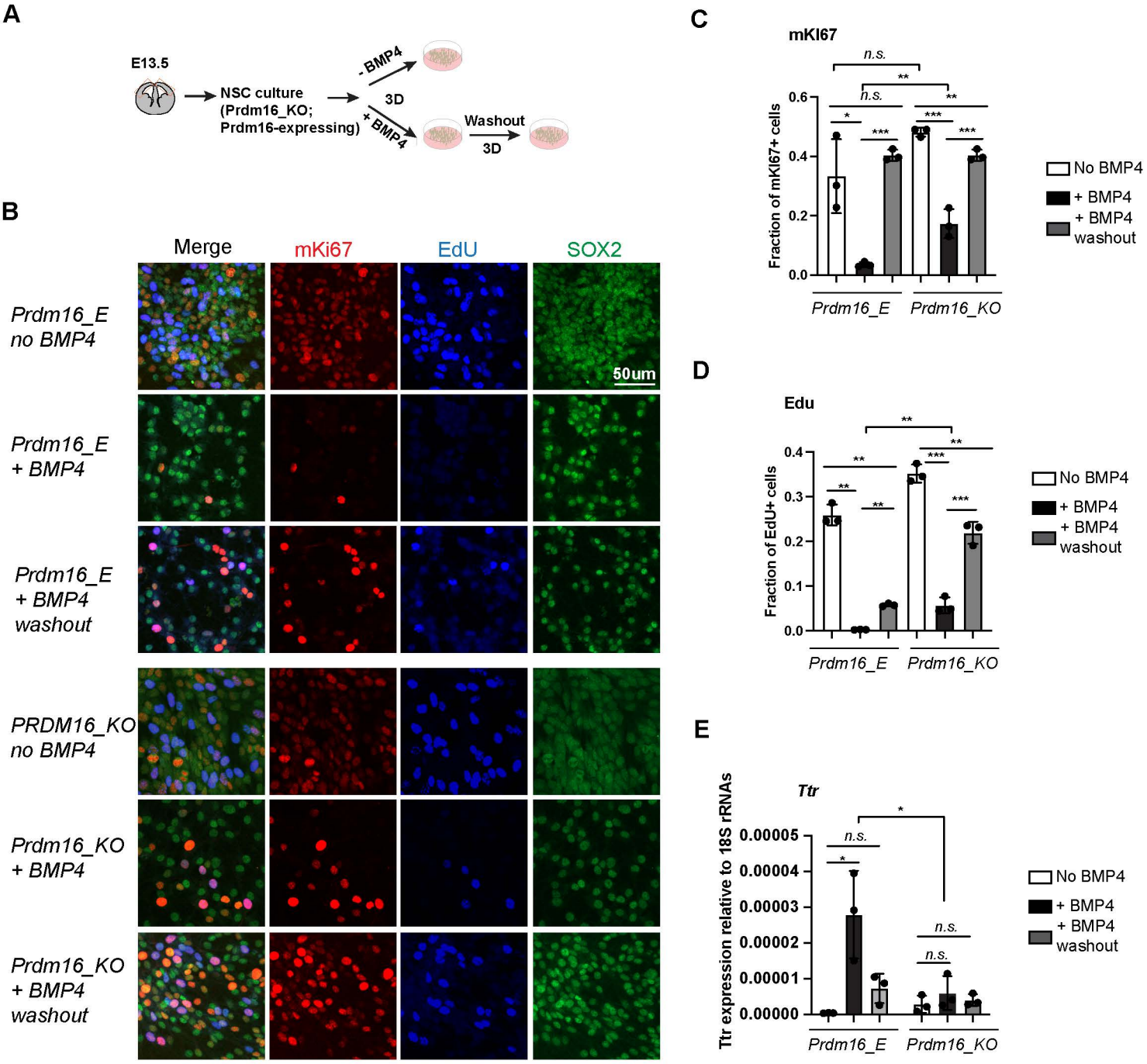
A
E13.5
NSC culture
(Prdm16_KO;
Prdm16-expressing)
- BMP4
3D
+ BMP4
Washout
3D
B
Merge
mKi67
EdU
SOX2
Prdm16_E
no BMP4
Prdm16_E
+ BMP4
Prdm16_E
+ BMP4
washout
PRDM16_KO
no BMP4
Prdm16_KO
+ BMP4
Prdm16_KO
+ BMP4
washout
50um
C
mKI67
Fraction of mKI67+ cells
Prdm16_E
Prdm16_KO
No BMP4
+ BMP4
+ BMP4
washout
D
Edu
Fraction of EdU+ cells
Prdm16_E
Prdm16_KO
No BMP4
+ BMP4
+ BMP4
washout
E
Ttr
Ttr expression relative to 18S rRNAs
Prdm16_E
Prdm16_KO
No BMP4
+ BMP4
+ BMP4
washout

Figure 2. *Prdm16* is required for BMP4-induced NSC quiescence

(**A**) Illustration of the NSC culture assay. (**B**) Immunostaining of mKI67 in red and SOX2 in green and EdU labeling in blue on indicated NSC genotypes and treatment. (**C**-**D**) Quantification of the fraction of mKI67+ (C) and EdU+ (D) cells among the total cell number marked by SOX2. (**E**) RT-qPCR measurement of *Ttr* levels relative to 18S RNAs. Biological replicates: N=3. Error bars represent standard deviation (SD). Statistical significance is calculated using unpaired t-test. ***, $p<0.001$; **, $p< 001$; *, $p<0.05$; n.s., non-significant

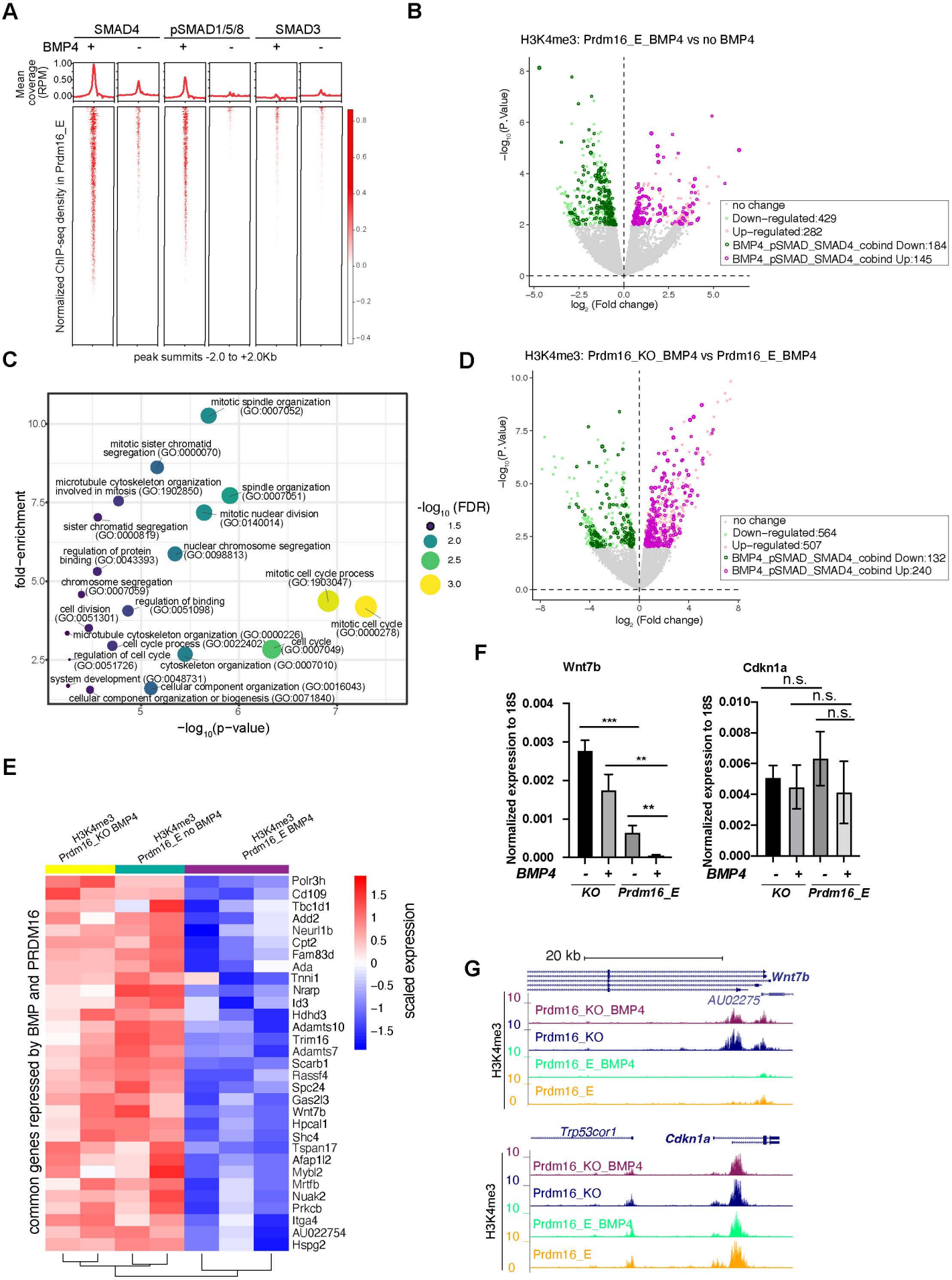
A
SMAD4
pSMAD1/5/8
SMAD3
BMP4 + - + - + -
Mean coverage (RPM)
Normalized ChIP-seq density in Prdm16_E
peak summits -2.0 to +2.0Kb
B
H3K4me3: Prdm16_E_BMP4 vs no BMP4
−log10(P.Value)
log2 (Fold change)
no change
Down−regulated:429
Up−regulated:282
BMP4_pSMAD_SMAD4_cobind Down:184
BMP4_pSMAD_SMAD4_cobind Up:145
C
fold−enrichment
−log10(p−value)
-log10 (FDR)
mitotic spindle organization (GO:0007052)
mitotic sister chromatid segregation (GO:0000070)
microtubule cytoskeleton organization involved in mitosis (GO:1902850)
spindle organization (GO:0007051)
mitotic nuclear division (GO:0140014)
sister chromatid segregation (GO:0000819)
regulation of protein binding (GO:0043393)
nuclear chromosome segregation (GO:0098813)
mitotic cell cycle process (GO:1903047)
chromosome segregation (GO:0007059)
regulation of binding (GO:0051098)
cell division (GO:0051301)
mitotic cell cycle (GO:0000278)
microtubule cytoskeleton organization (GO:0000226)
cell cycle process (GO:0022402)
cell cycle (GO:0007049)
regulation of cell cycle (GO:0051726)
cytoskeleton organization (GO:0007010)
system development (GO:0048731)
cellular component organization (GO:0016043)
cellular component organization or biogenesis (GO:0071840)
D
H3K4me3: Prdm16_KO_BMP4 vs Prdm16_E_BMP4
−log10(P.Value)
log2 (Fold change)
no change
Down−regulated:564
Up−regulated:507
BMP4_pSMAD_SMAD4_cobind Down:132
BMP4_pSMAD_SMAD4_cobind Up:240
E
H3K4me3 Prdm16_KO BMP4
H3K4me3 Prdm16_E no BMP4
H3K4me3 Prdm16_E BMP4
common genes repressed by BMP and PRDM16
scaled expression
Polr3h
Cd109
Tbc1d1
Add2
Neurl1b
Cpt2
Fam83d
Ada
Tnni1
Nrarp
Id3
Hdhd3
Adamts10
Trim16
Adamts7
Scarb1
Rassf4
Spc24
Gas2l3
Wnt7b
Hpcal1
Shc4
Tspan17
Afap1l2
Mybl2
Mrtfb
Nuak2
Prkcb
Itga4
AU022754
Hspg2
F
Wnt7b
Cdkn1a
Normalized expression to 18S
BMP4
KO
Prdm16_E
n.s.
G
20 kb
Wnt7b
AU02275
H3K4me3
Prdm16_KO_BMP4
Prdm16_KO
Prdm16_E_BMP4
Prdm16_E
Trp53cor1
Cdkn1a

Figure 3. BMP signaling represses cell proliferation genes to induce cell quiescence

(**A**) Heatmaps of ChIP-seq coverage (normalized by library depths and input) centered at peak summits for SMAD4, pSMAD1/5/8 and SMAD3 in *Prdm16_E* cells with or without BMP4. (**B**) A volcano plot of differential H3K4me3 read counts at TSS in *Prdm16_E* cells with BMP4 versus those with no BMP4. Significant changes ($P < 0.01$) are colored. (**C**) A bubble plot showing GO terms significantly enriched in SMAD-repressed genes (labelled in dark green in B). (**D**) A volcano plot of differential H3K4me3 read counts at TSS in *Prdm16_KO* cells with BMP4 versus *Prdm16_E* cells with BMP4. Significant changes ($P < 0.01$) are colored. **(E)** A heatmap of H3K4me3 normalized read counts at TSS of the 31 genes co-repressed by PRDM16 and SMADs (overlapping genes from those in dark green in B and those in dark pink in D). (**F**) RT-qPCR measurement of *Wnt7b* and *Cdkn1a* mRNA levels in indicated genotypes and conditions from three biological replicates, each with two technical replicates. Statistical significance was calculated using unpaired t-test (***, $p<0.001$; **, $p< 0.01$; *, $p<0.05$; n.s., non-significant). (**G**) Genome browser snapshots showing the H3K4me3 CUT&TAG tracks in the *Wnt7b* and *Cdkn1a* loci.

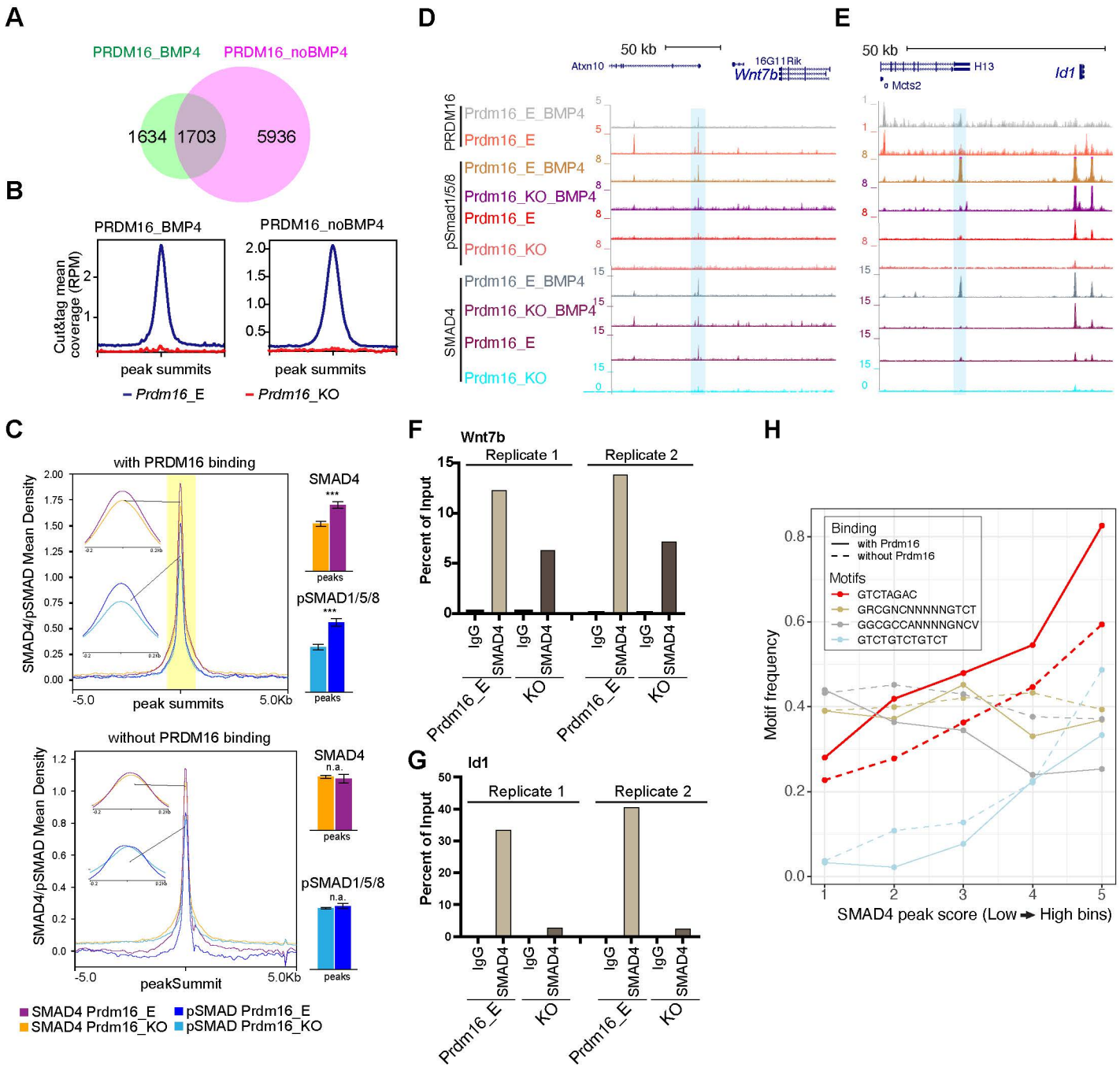
A
PRDM16_BMP4
PRDM16_noBMP4
1634
1703
5936
B
PRDM16_BMP4
PRDM16_noBMP4
Cut&tag mean coverage (RPM)
peak summits
Prdm16_E
Prdm16_KO
C
with PRDM16 binding
SMAD4/pSMAD Mean Density
peak summits
SMAD4
pSMAD1/5/8
peaks
without PRDM16 binding
peakSummit
n.a.
SMAD4 Prdm16_E
SMAD4 Prdm16_KO
pSMAD Prdm16_E
pSMAD Prdm16_KO
D
50 kb
Atxn10
16G11Rik
Wnt7b
PRDM16
Prdm16_E_BMP4
Prdm16_E
pSmad1/5/8
Prdm16_KO_BMP4
Prdm16_KO
SMAD4
E
H13
Id1
Mcts2
F
Wnt7b
Replicate 1
Replicate 2
Percent of Input
IgG
SMAD4
Prdm16_E
KO
G
Id1
H
Binding
with Prdm16
without Prdm16
Motifs
GTCTAGAC
GRCGNCNNNNNGTCT
GGCGCCANNNNGNCV
GTCTGTCTGTCT
Motif frequency
SMAD4 peak score (Low → High bins)

Figure 4. PRDM16 anchors the SMAD proteins at specific genomic regions to mediate repression

(**A)** A Venn diagram showing the overlap of CUT&TAG peak in BMP4-treated and non-treated Prdm16_E cells. **(B)** The mean coverages (normalized by library depths) centered at peak summits are shown for the PRDM16 CUT&TAG signal in BMP4-treated and non-treated *Prdm16_E* cells and Prdm16_KO mutant samples (4 replicates combined). **(C)** Metaplots of SMAD4 and pSMAD1/5/8 ChIP-seq coverage centered at SMAD or pSMAD peak summits that have PRDM16 co-binding (top) and those without PRDM16 co-binding (bottom) in BMP4 treated *Prdm16_E* and *Prdm16_KO* cells. The average coverage is plotted in the bar plots on the right. Only the peaks with PRDM16 co-binding show significant reduction in the KO cells (*** $P<0.001$; ** $P<0.01$; * $P<0.05$; n.a. $P>0.05$). **(D-E)** Genome browser view of the *Wnt7b* and *Id1* loci, showing PRDM16 CUT&TAG and SMAD ChIP-seq tracks. The co-bound regions are highlighted. **(F-G)** ChIP-qPCR validation of SMAD4 binding to the highlighted regions in D-E from *Prdm16_E* and *Prdm16_KO* cells with two replicates. (**H**) The occurrence frequency of four types of SMAD motifs is shown in five binned SMAD ChP-seq peaks scored from low to high. The palindromic motif GTCTAGAC shows the highest occurrence frequency in peaks with PRDM16 co-binding (solid red) and is the only one that has reduced occurrence frequency in peaks without PRDM16 co-binding (dashed red).

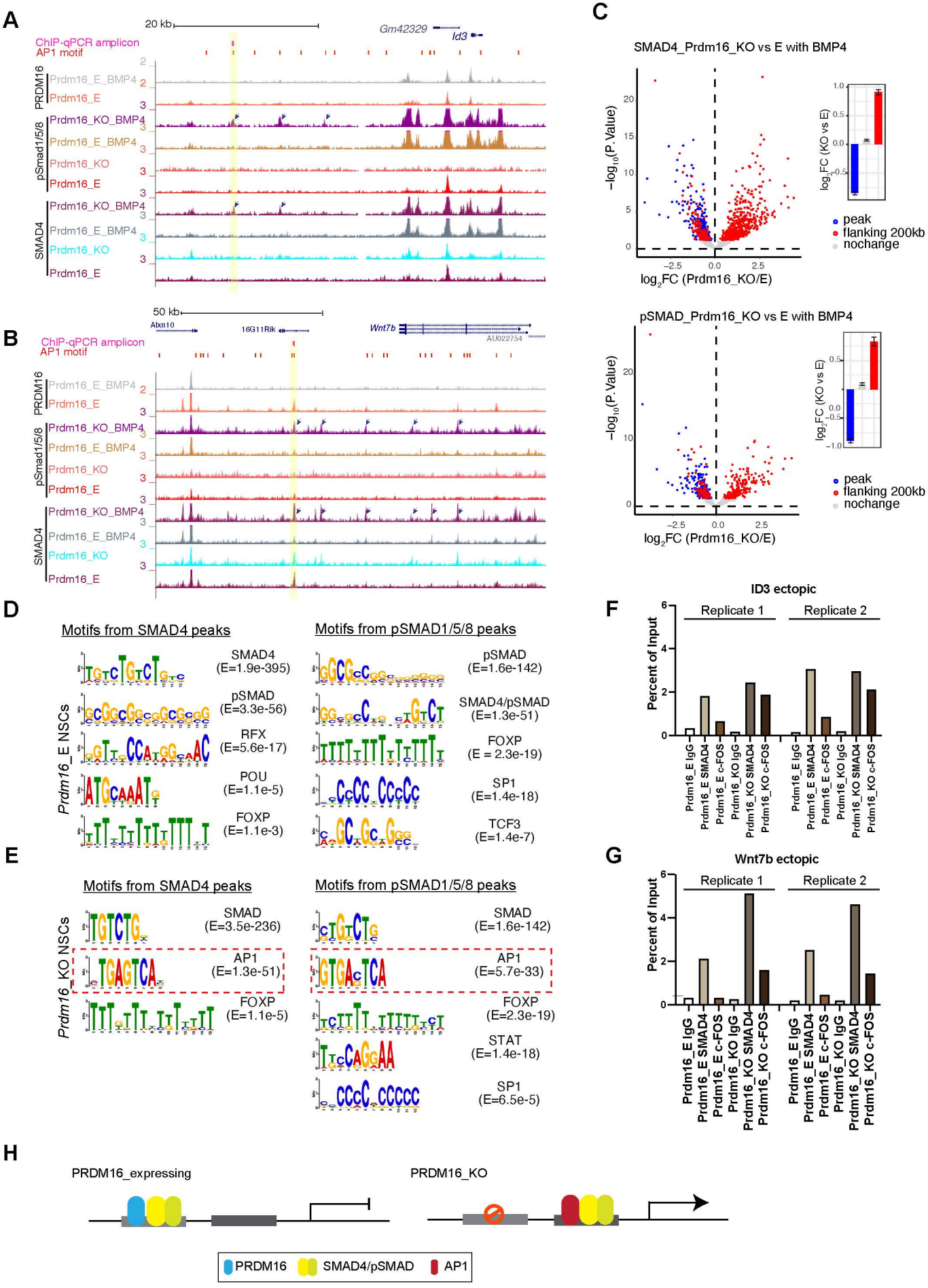
A
20 kb
Gm42329
Id3
ChIP-qPCR amplicon
AP1 motif
PRDM16
Prdm16_E_BMP4
Prdm16_E
pSmad1/5/8
Prdm16_KO_BMP4
Prdm16_E_BMP4
Prdm16_KO
Prdm16_E
SMAD4
Prdm16_KO_BMP4
Prdm16_E_BMP4
Prdm16_KO
Prdm16_E
B
50 kb
Abxn10
16G11Rik
Wnt7b
AU022754
ChIP-qPCR amplicon
AP1 motif
PRDM16
Prdm16_E_BMP4
Prdm16_E
pSmad1/5/8
Prdm16_KO_BMP4
Prdm16_E_BMP4
Prdm16_KO
Prdm16_E
SMAD4
Prdm16_KO_BMP4
Prdm16_E_BMP4
Prdm16_KO
Prdm16_E
C
SMAD4_Prdm16_KO vs E with BMP4
−log10(P.Value)
log2FC (Prdm16_KO/E)
log2FC (KO vs E)
peak
flanking 200kb
nochange
pSMAD_Prdm16_KO vs E with BMP4
−log10(P.Value)
log2FC (Prdm16_KO/E)
log2FC (KO vs E)
peak
flanking 200kb
nochange
D
Motifs from SMAD4 peaks
Motifs from pSMAD1/5/8 peaks
Prdm16_E NSCs
SMAD4 (E=1.9e-395)
pSMAD (E=3.3e-56)
RFX (E=5.6e-17)
POU (E=1.1e-5)
FOXP (E=1.1e-3)
pSMAD (E=1.6e-142)
SMAD4/pSMAD (E=1.3e-51)
FOXP (E = 2.3e-19)
SP1 (E=1.4e-18)
TCF3 (E=1.4e-7)
E
Motifs from SMAD4 peaks
Motifs from pSMAD1/5/8 peaks
Prdm16_KO NSCs
SMAD (E=3.5e-236)
AP1 (E=1.3e-51)
FOXP (E=1.1e-5)
SMAD (E=1.6e-142)
AP1 (E=5.7e-33)
FOXP (E=2.3e-19)
STAT (E=1.4e-18)
SP1 (E=6.5e-5)
F
ID3 ectopic
Replicate 1
Replicate 2
Percent of Input
Prdm16_E IgG
Prdm16_E SMAD4
Prdm16_E c-FOS
Prdm16_KO IgG
Prdm16_KO SMAD4
Prdm16_KO c-FOS
G
Wnt7b ectopic
Replicate 1
Replicate 2
Percent of Input
Prdm16_E IgG
Prdm16_E SMAD4
Prdm16_E c-FOS
Prdm16_KO IgG
Prdm16_KO SMAD4
Prdm16_KO c-FOS
H
PRDM16_expressing
PRDM16_KO
PRDM16
SMAD4/pSMAD
AP1

Figure 5. The SMAD complex switches genome localization in the absence of Prdm16

(**A-B**) Genome browser snapshots of the *Id3* (top) and *Wnt7b* (bottom) gene loci, showing ectopic SMAD peaks, indicated by the arrows. **(C)** The volcano plots showing differential SMAD4 and pSMAD1/5/8 ChIP-seq read counts in BMP4-treated *Prdm16_KO* cells compared to BMP4-treated *Prdm16_E* cells. The sites in blue are co-bound by PRDM16, while the sites in red are not bound by PRDM16 but within the 200kb of a PRDM16-cobound site. The average log2 fold-change is plotted on the right. (**D-E**) *De novo* motif discovery from SMAD4 and pSMAD1/5/8 ChIP-seq peaks in *Prdm16_E* cells (**D**) and *Prdm16_KO* cells (**E**). (**F-G**) ChIP-qPCR validation of increased SMAD4 and c-FOS occupancy at the highlighted ectopic sites in *Prdm16_KO* mutant cells versus *Prdm16_E* cells. The locations of PCR amplicons are shown in A and B. **(H)** An enhancer switch model demonstrating that SMADs change co-factors and become into a transcriptional activator in the absence of PRDM16.

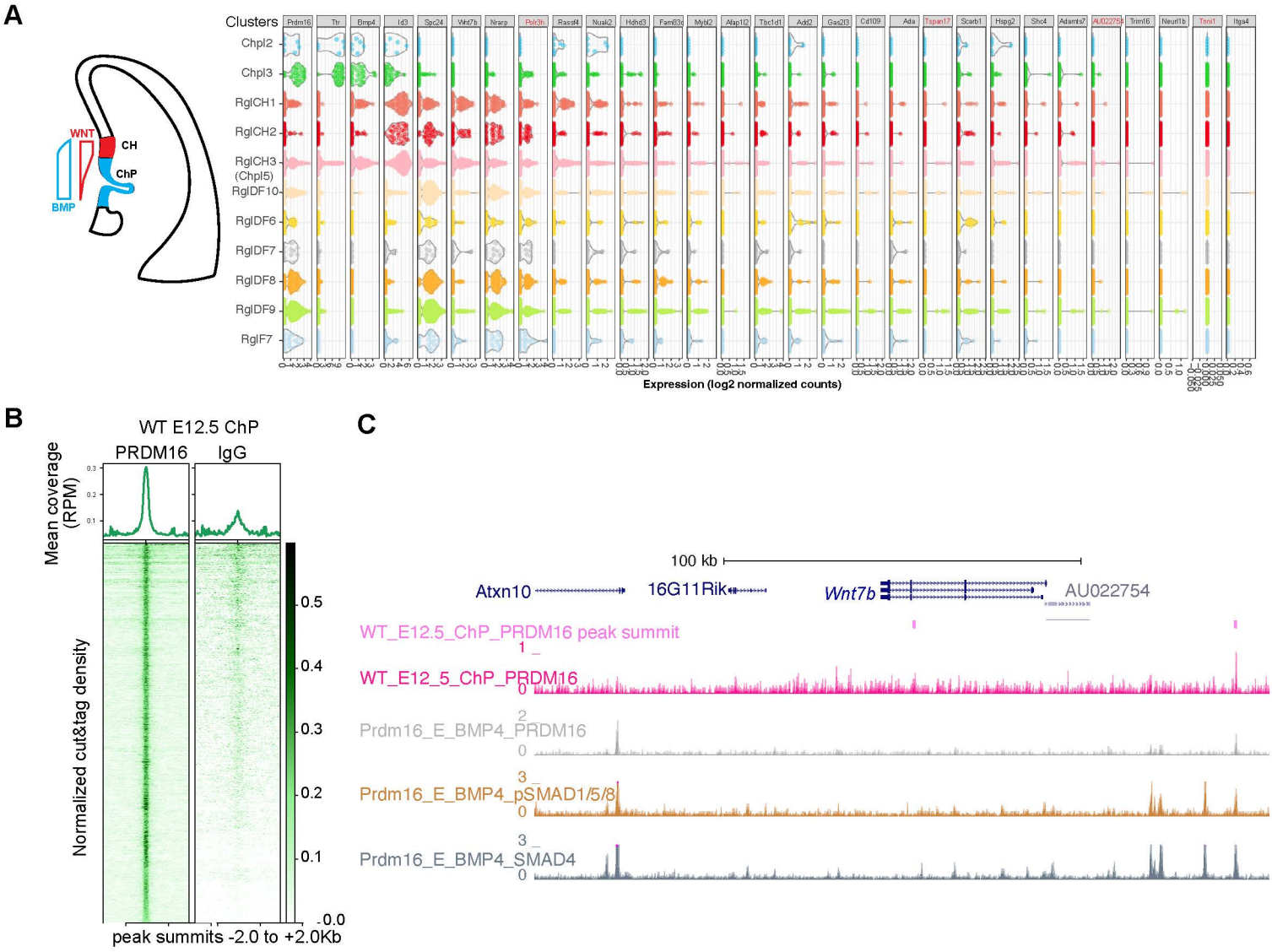
A
WNT
CH
ChP
BMP
Clusters
Chpl2
Chpl3
RglCH1
RglCH2
RglCH3
(Chpl5)
RglDF10
RglDF6
RglDF7
RglDF8
RglDF9
RglF7
Expression (log2 normalized counts)
B
WT E12.5 ChP
PRDM16
IgG
Mean coverage
(RPM)
Normalized cut&tag density
peak summits -2.0 to +2.0Kb
C
100 kb
Atxn10
16G11Rik
Wnt7b
AU022754
WT_E12.5_ChP_PRDM16 peak summit
WT_E12_5_ChP_PRDM16
Prdm16_E_BMP4_PRDM16
Prdm16_E_BMP4_pSMAD1/5/8
Prdm16_E_BMP4_SMAD4

Figure 6. PRDM16 and SMADs co-regulated genes are differentially expressed in the ChP and neural cells

(**A**) An illustration of the CH and ChP regions with opposite Wnt and BMP gradients and a violin plot of scRNA-seq gene expression at E12.5 for the indicated genes in several selected cell type clusters reanalyzed from [37]. Definition of the clusters is based on marker gene expression from E9.5-E18.5 brain cells. These include the choroid plexus clusters 1-5 (Chpl), with cluster Chpl5 identified by this study based on *Ttr* expression, Radial glia clusters (RglCH 1-3, RglDF 6-10, and RglF7). CH: cortical hem; DF: dorsal forebrain; F: forebrain. Per cell expression was normalized to give a log2 normalized counts. **(B)** Metaplots and heatmaps of PRDM16 and IgG CUT&TAG coverage (normalized by library depths) centered at peak summits from E12.5 dorsal midline tissues. **(C)** A genome browser snapshot of the *Wnt7b* locus, showing PRDM16 CUT&TAG and SMADs ChIP-seq tracks.

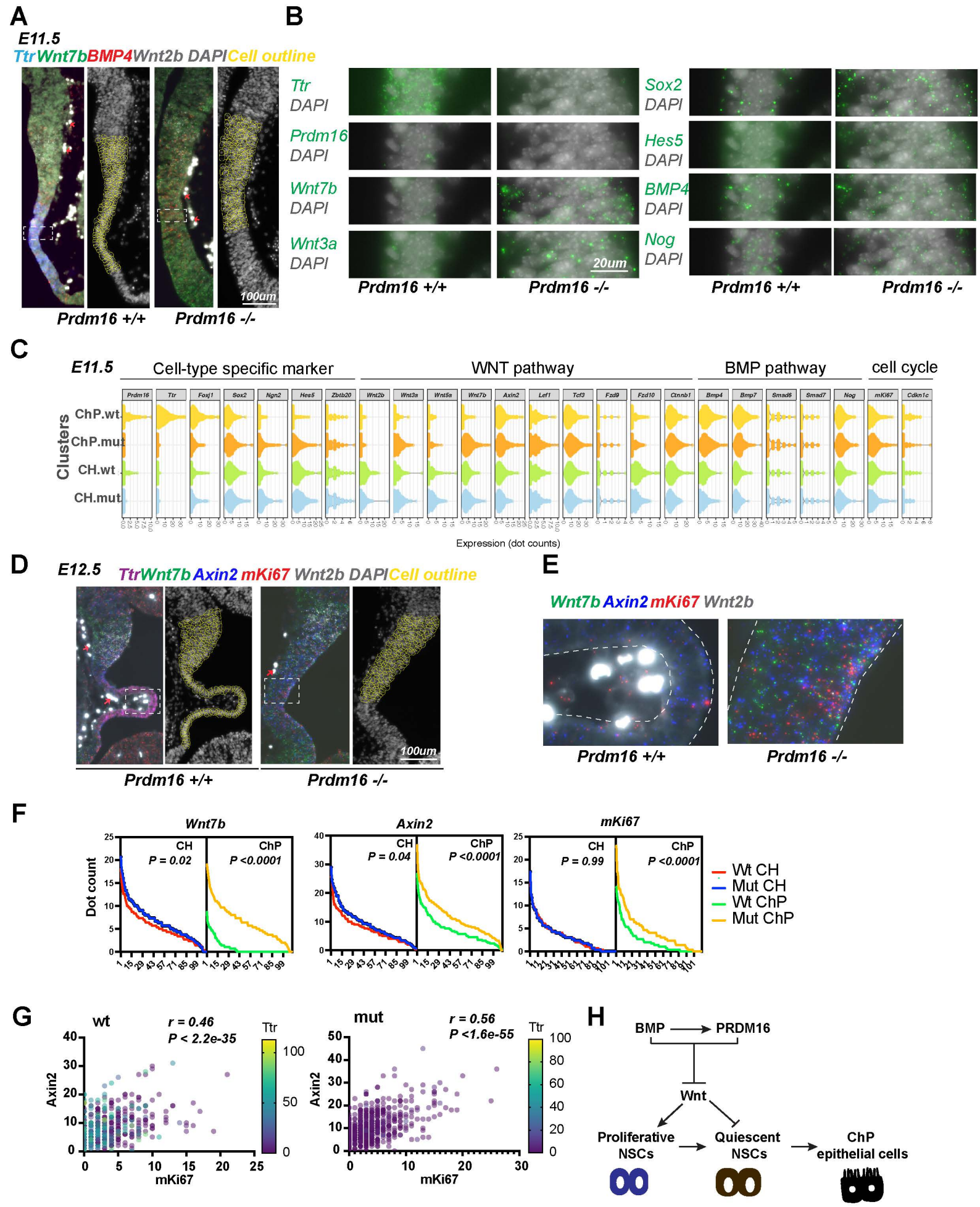
A
E11.5
Ttr Wnt7b BMP4 Wnt2b DAPI Cell outline
100um
Prdm16 +/+
Prdm16 -/-
B
Ttr DAPI
Prdm16 DAPI
Wnt7b DAPI
Wnt3a DAPI
Sox2 DAPI
Hes5 DAPI
BMP4 DAPI
Nog DAPI
20um
Prdm16 +/+
Prdm16 -/-
Prdm16 +/+
Prdm16 -/-
C
E11.5
Cell-type specific marker
WNT pathway
BMP pathway
cell cycle
Prdm16 Ttr Foxj1 Sox2 Ngn2 Hes5 Zbtb20 Wnt2b Wnt3a Wnt5a Wnt7b Axin2 Lef1 Tcf3 Fzd9 Fzd10 Ctnnb1 Bmp4 Bmp7 Smad6 Smad7 Nog mKi67 Cdkn1c
Clusters
ChP.wt
ChP.mut
CH.wt
CH.mut
Expression (dot counts)
D
E12.5
Ttr Wnt7b Axin2 mKi67 Wnt2b DAPI Cell outline
100um
Prdm16 +/+
Prdm16 -/-
E
Wnt7b Axin2 mKi67 Wnt2b
Prdm16 +/+
Prdm16 -/-
F
Wnt7b
Axin2
mKi67
Dot count
CH
P = 0.02
ChP
P <0.0001
CH
P = 0.04
ChP
P <0.0001
CH
P = 0.99
ChP
P <0.0001
Wt CH
Mut CH
Wt ChP
Mut ChP
G
wt
r = 0.46
P < 2.2e-35
Ttr
Axin2
mKi67
mut
r = 0.56
P <1.6e-55
Ttr
Axin2
mKi67
H
BMP
PRDM16
Wnt
Proliferative NSCs
Quiescent NSCs
ChP epithelial cells

Figure 7. PRDM16 suppresses Wnt signaling and cell proliferation in ChP epithelial cells

(**A**) SCRINSHOT images of E11.5 wild-type and *Prdm16* mutant brains, with *BMP4*, *Ttr*, *Wnt7b* and *Wnt2b* probes. Note: The red arrows indicate a strong unspecific signal in all channels due to autofluorescence of blood cells. The cells selected for quantification are highlighted in yellow in the DAPI channel. (**B**) Enlarged views of SCRINSHOT images at the area indicated in A, showing an increase of Wnt and neural gene expression levels and decrease of *Ttr* and *Prdm16*. (**C**) A violin plot with the dot counts measuring expression levels of the 24 genes examined. Each gene is measured in 330 CH and 330 ChP cells from three wild-type and three Prdm16 mutant samples. (**D**) SCRINSHOT images for E12.5 wild-type and Prdm16 mutant brains, with Axin2, Ttr, Wnt 7b, Wnt2b and mKi67 probes. (**E**) Enlarged views of the areas indicated in the dash-lined rectangles in D. The ChP parts are highlighted by dashed lines. (**F**) Distribution of dot counts for indicated genes in the wild-type (*wt*) and *Prdm16* mutant (*mut*) CH and ChP areas. The X-axis shows the 110 cells in each replicate, and the Y-axis shows the mean value of the number of counts in three biological replicates. P value was calculated using area under the ROC curve in Prism Graphpad. (**G**) Multi-variant linear regression of *mKi67*, *Axin2* and *Ttr* using the dot counts for each gene in three pairs of wild-type and *Prdm16* mutant samples. All 660 cells including both CH and ChP tissues in each genotype are included. Pearson correlation and statistical difference were calculated in Prism Graphpad. (H) Illustration of the regulatory circuit, which is required for transitioning proliferative NSCs to quiescent NSCs, a prerequisite for the specification of ChP epithelial cells.